A Formulation of Directivity for Earthquake Sources Using Isochrone Theory

By Paul Spudich,[1] Brian S.J. Chiou,[2] Robert Graves,[3]
Nancy Collins,[3] *and* Paul Somerville,[3]

Open-File Report 2004–1268

2004

U.S. DEPARTMENT OF THE INTERIOR
U.S. GEOLOGICAL SURVEY

[1] U.S. Geological Survey, MS 977, 345 Middlefield Road, Menlo Park, CA 94025
[2] California Department of Transportation, 5900 Folsom Blvd, MS 5, Sacramento, CA 95819.
[3] URS Corporation, 566 El Dorado Street, Pasadena, CA 91101-2560.

Table of Contents

ABSTRACT

A functional form for directivity effects can be derived from isochrone theory, in which the measure of the directivity-induced amplification of an S body wave is c,the isochrone velocity. Ground displacement of the near-, intermediate-, and far-field terms of P and S waves is linear in isochrone velocity for a finite source in a whole space. We have developed an approximation $\tilde{c}'$ of isochrone velocity that can easily be implemented as a predictor of directivity effects in empirical ground motion prediction relations. Typically, for a given fault surface, hypocenter, and site geometry, $\tilde{c}'$ is a simple function of the hypocentral distance, the rupture distance, the crustal shear wave speed in the seismogenic zone, and the rupture velocity. $\tilde{c}'$ typically ranges in the interval 0.44, for rupture away from the station, to about 4, for rupture toward the station. In this version of the theory directivity is independent of period. Additionally, we have created another functional form which is $\tilde{c}'$ modified to include the approximate radiation pattern of a finite fault having a given rake. This functional form can be used to model the spatial variations of fault-parallel and fault-normal horizontal ground motions. The strengths of this formulation are 1) the proposed functional form is based on theory, 2) the predictor is unambiguously defined for all possible site locations and source rakes, and 3) it can easily be implemented for well-studied important previous earthquakes. We compare predictions of our functional form with synthetic ground motions calculated for finite strike-slip and dip-slip faults in the magnitude range 6.5 - 7.5. In general our functional form correlates best with computed fault-normal and fault-parallel motions in the synthetic motions calculated for events with M6.5. Correlation degrades but is still useful for larger events and for the geometric average horizontal motions. We have had limited success applying it to geometrically complicated faults.

THEORETICAL DEVELOPMENT

The measure of directivity in isochrone theory is c, isochrone velocity. Ground displacement of the near-, intermediate-, and far-field terms of P and S waves is linear in c, isochrone velocity, for a finite source in a wholespace (Joyner and Spudich, 1988). Spudich and Frazer (1984, 1987) have applied the concept of isochrone velocity to an Earth structure that varies with depth. An interesting early application of isochrone theory to ground motion prediction relations was made by Rogers and Perkins (1996). Isochrone velocity is defined by

$$c := \left| \underline{\nabla}_s t_a(\mathbf{x},\mathbf{x}_s) \right|^{-1}$$

where $\mathbf{x}_s$ is the station location, $\mathbf{x}$ is a location on the fault, $t_a(\mathbf{x},\mathbf{x}_s)$ is the arrival time at $\mathbf{x}_s$ of a P or S wave radiated from the rupturing of point $\mathbf{x}$, and $\underline{\nabla}_s$ is the vector surface gradient function. In this document we use S waves exclusively. Arrival time is defined as the sum of the rupture time $t_r(\mathbf{x})$ and the S-wave travel time t_S,

$$t_a(\mathbf{x},\mathbf{x}_s) = t_r(\mathbf{x}) + t_S(\mathbf{x},\mathbf{x}_s) \qquad (1)$$

and we assume that the rupture propagates at uniform rupture velocity v_r, so

$$t_r(\mathbf{x}) = \left|\mathbf{x} - \mathbf{x}_h\right| / v_r\,, \qquad (2)$$

where $\mathbf{x}_h$ is the hypocenter location. We **explicitly assume** $v_r < \beta$**,** where β is the shear wave speed in the source region.

An example calculation is shown in Figure 1. These calculations and plots were made using the ISOSYN software of Spudich and Xu (2003). The fault is a vertical strike-slip fault 170 km long and 17 km wide, with a station located 1 km off the fault at -30 km along strike. $\mathbf{x}_c$ is the point on the fault closest to station. (This example is modeled on station 09 for the strike-slip event SG in the "1D rock simulations" of Abrahamson, 2003.) The S velocity structure is uniform except for a low S velocity in the top 1 km of the structure. Figure 1a shows contours of rupture time $t_r(\mathbf{x})$ for a uniformly expanding circular rupture. (Note the 10:1 vertical exaggeration.) The slip distribution in this simple example is uniform with a tapering zone at the fault edges. Figure 1b shows the S wave travel time function t_S on the fault. Figure 1c shows the isochrones, the contours of the arrival time function $t_a(\mathbf{x},\mathbf{x}_s)$, which is the sum of the rupture time from Figure 1a and the S travel time from Figure 1b. The arrival time function shows the time that S waves from each point on the rupture arrive at the station. For example, the S from the hypocenter arrives at about 25.5 s after the origin time; S waves from the upper right corner of the fault arrive at the station about 44 s after the origin time, and S waves from $\mathbf{x}_c$ arrive about 32 s after the origin time. The colors in Figure 1c show the isochrone velocity at each point on the fault. The isochrone velocity is the spacing between two adjacent isochrones divided by their arrival time difference. Ground motions are proportional to isochrone velocity for the following reason. Consider the portion of the fault between the 26 s and 32 s contours. All the S waves from this section of the fault arrive at the station within a 6 s window. Now consider the part of the fault between the 32 and the 38 s contours. All these S waves also arrive in a 6 s duration window. Clearly a much larger part of the fault contributes S waves during the 26-32 s window than during the 32-38 s window, so the ground motions are bigger during the 26-32 s window. This is the kinematic explanation of directivity.

Approximations of Isochrone Velocity

Let $\mathbf{x}_c$ be the point on the fault closest to a station at $\mathbf{x}_s$, so that rupture distance $r_r = |\mathbf{x}_c - \mathbf{x}_s|$. Here $r_r = r_{rup}$ is the "rupture distance" commonly used in engineering practice (Abrahamson and Shedlock, 1997). Numerical simulations show that the largest radiated motions tend to come from the part of the fault in which rupture advances toward $\mathbf{x}_c$, i.e. the region between the hypocenter at $\mathbf{x}_h$ and $\mathbf{x}_c$. For this portion of the fault, a good approximation of c is $\tilde{c}$ (Figure 2),

$$\tilde{c} := \frac{|\mathbf{x}_c - \mathbf{x}_h|}{t_a(\mathbf{x}_c) - t_a(\mathbf{x}_h)} = \frac{D}{t_a(\mathbf{x}_c) - t_a(\mathbf{x}_h)} \tag{3}$$

where $t_a(\mathbf{x}_c)$ and $t_a(\mathbf{x}_h)$ are actually functions of some or all of $\mathbf{x}_c, \mathbf{x}_s,$ and $\mathbf{x}_h$, but we suppress extraneous arguments to reduce clutter. $\tilde{c}$ is easily derived from parameters usually available to attenuation relation developers, as will be shown below.

The distance D on the fault from $\mathbf{x}_h$ to $\mathbf{x}_c$ is

$$D = |\mathbf{x}_c - \mathbf{x}_h| = \sqrt{s^2 + d^2} = \sqrt{L^2 X^2 + W^2 Y^2} \tag{4}$$

where s and d are the Somerville et al. (1997) distances, as shown in Figure 2. L and W are the length and width of the rectangular slip zone, and X and Y are s/L and d/W, as in Somerville et al. (1997). In the following we assume straight S ray paths, but equation (3) is valid for curving rays in any 3D velocity structure.

We can show that $\tilde{c}$ is a good approximation of c using our computed example in Figure 1c. In that case $t_a(\mathbf{x}_c) - t_a(\mathbf{x}_h)$ = 32 - 25.5 s = 6.5 s. D, the distance between $\mathbf{x}_h$ and $\mathbf{x}_c$ is about 87 km, so $\tilde{c}$ = 87 / 6.5 km/s = 13.4 km/s. Looking at the streak of green in Figure 1c, we can see that the actual isochrone velocity between the hypocenter and the closest point is about 15 km/s. Thus the simple expression in (3) for $\tilde{c}$ is a good approximation of c for the part of the rupture between the hypocenter and the closest point.

For practical use we must express $\tilde{c}$ in terms of quantities typically available in engineering practice. Now

$$t_a(\mathbf{x}_c) = t_r(\mathbf{x}_c) + t_S(\mathbf{x}_c) = D/v_r + r_r/\beta \tag{5}$$

$$t_a(\mathbf{x}_h) = r_h/\beta \tag{6}$$

where $r_h = |\mathbf{x}_s - \mathbf{x}_h|$ is hypocentral distance.

$$\therefore t_a(\mathbf{x}_c) - t_a(\mathbf{x}_h) \quad = \quad \frac{1}{\beta}\left(\frac{D}{v_r/\beta} + r_r - r_h\right), \text{ and} \tag{7}$$

$$\tilde{c} \quad = \quad \beta\left(\frac{\beta}{v_r} + D^{-1}(r_r - r_h)\right)^{-1}. \tag{8}$$

Isochrone Velocity Ratio - The Useful Expression

Because the physical phenomenon of directivity is a function of v_r/β, it is sensible to normalize $\tilde{c}$ by local shear wave velocity β (Appendix A). Thus, a better measure of directivity is the isochrone velocity ratio $\tilde{c}/\beta$

$$\tilde{c}' := \tilde{c}/\beta \quad = \quad \left(\frac{\beta}{v_r} + D^{-1}(r_r - r_h)\right)^{-1}, \quad D > 0. \tag{9a}$$

$$\quad = \quad \frac{v_r}{\beta}, \quad D = 0. \tag{9b}$$

$\tilde{c}'$ is the term closest to $\cos(\theta)$ and $\cos(\phi)$ of Somerville et al (1997). $\tilde{c}'$ has an angular behavior similar to $\cos(\theta)$ and $\cos(\phi)$ because $t_a(\mathbf{x}_c) - t_a(\mathbf{x}_h)$ is smallest when the station is in the forward direction and largest when the station is perpendicular to the hypocenter. It has the advantage of being appropriate for any geometry of

$\mathbf{x}_c$, $\mathbf{x}_s$, and $\mathbf{x}_h$, combining into one term the two terms $\cos(\theta)$ and $\cos(\phi)$. A potential problem of $\tilde{c}'$ is that it can be singular when rupture velocity approaches the S-wave velocity. $\tilde{c}'$ lies in the range

$$\frac{v_r}{\beta} \le \tilde{c}' \le \left(\frac{\beta}{v_r} - 1\right)^{-1}$$

which, for $v_r/\beta = 0.8$ is the range from 0.8 to 4. Caution may be needed when $v_r/\beta > 0.8$. When nothing is known about the rupture velocity of the earthquakes being studied, it is probably reasonable to assume that $v_r/\beta = 0.8$ (Heaton, 1990); limited testing of our theory with synthetic seismograms calculated for the source geometries specified in Abrahamson (2003) indicates that this assumption is acceptable.

Like the $X\cos(\theta)$ term of Somerville et al. (1997), the above derivation assumes that the earthquake source has bilateral rupture, i.e. the hypocenter is not on the edge of the fault. For bilateral sources with a circular rupture front, some part of the fault is rupturing toward every station, except those stations exactly perpendicular to the hypocenter. If a source is truly unilateral , i.e. the hypocenter is at the edge of a fault, then some stations can be in the backward direction. For stations in the backward direction, we derive a back-direction isochrone velocity ratio $\tilde{c}'_b$,

$$\tilde{c}'_b \;:=\; \left(\frac{\beta}{v_r} + 1\right)^{-1} \quad \approx 0.44 \text{ for } v_r/\beta = 0.8. \qquad (10)$$

This expression was derived for a line source rupturing directly away from the station. $\tilde{c}'_b$ is the minimum possible value of $\tilde{c}'$, A use of this term is given below.

Modification for Fault Edge Effects

There are two reasons why $\tilde{c}'$ should be modified to account for fault edge effects. First, we note that slip in earthquakes tends to taper to zero at the edges of faults over some distance a_s along strike and a_d along the dip direction. Clearly if $\mathbf{x}_c$ is on the edge of the fault and $D < a_s$ (or a_d as appropriate), less ground motion will result. The widths a_s along strike and a_d along dip can be taken from actual widths of zones of tapering slip at the edges of faults. We equate a_s and a_d with half the correlation distances ($a_x/2$ and $a_z/2$, respectively) of Mai & Beroza (2002), For rupture models derived from strong motion and geodetic inversions they find $a_x \approx 2 + L_{eff}/3$ and $a_z \approx 1 + W_{eff}/3$, where L_{eff} and W_{eff} are their effective fault lengths and widths. Of course, their correlation distances might be broadened by the limited spatial resolution of the inversions. For simplicity we choose

$$\begin{aligned} a_s &= a_x/2 = L/6 \\ a_d &= a_z/2 = W/6 \end{aligned} \tag{11}$$

The use of $a_x/2$ and $a_z/2$ for a_s and a_d is reasonable because a_x is the correlation length and the wavenumber power spectrum of slip is down by a factor of 1/e when wavelength is a_s or a_d. Here we approximate that full slip is expected at some distance $a_x/2$ from the edge of the fault where slip is by definition zero. However, a_s and a_d might need to be raised for several reasons: 1) a 1/e decay might not be enough of a decay; perhaps $1/e^2$ would be better. Second, owing to finite slip rise times, isochrones are actually bands of finite width on the fault, and here we approximate them as lines. Finite bands would smooth over a larger part of the fault surface. The correct theoretical values of a_s and a_d are still not clear, and they might be a function of rise time (and thus, magnitude). However, in this report we do not modify $\tilde{c}'$ to account for slip tapering because we have not yet found a simple algorithm. In addition, the tapering of slip at the edges of faults would be more appropriately included in empirical regression relations by redefining the distance measure to omit low-slip peripheries of ruptures, similar to Campbell's use of r_{seis} rather than r_{rup} (=r_r here), if the low-slip peripheries are present in the fault lengths and widths of the earthquakes from which the regression relations are derived.

There is a second reason why we should modify $\tilde{c}'$ for the hypocenter's proximity to the edge of the fault, and in this work we make that modification. Consider the case in Figure 2 where D is 1 cm. In this geometry there is only 1 cm of forward rupture propagation toward station 1, but $\tilde{c}'$ can still be high at that station because $r_r - r_h$ decreases at the same rate as D in (9a) so that the limit is stable. In this case, the forward directivity pulse is confined between the S from the hypocenter and the S from the closest point on the fault, and these two arrival times might differ by only 10^{-5} s. Thus, in reality there is forward directivity, but it occurs only in a very brief pulse carrying very little moment. For that reason we have concocted an edge-modification factor m_5 which uses the arrival time difference between the hypocentral S and the S from the closest point as an indicator of proximity of the hypocenter to the closest point. This edge modification factor is described in Appendix B.

To include the edge modification factors, we define $c*$, which is $\tilde{c}'$ modified by the factor m_5. The simplest modification is a straight multiplication,

$$c_1*(\mathbf{x}_s) := m_5(\mathbf{x}_c, \mathbf{x}_h)\tilde{c}'. \tag{12}$$

$c*$ is unitless. Note that it is possible for c_1* to be zero for a hypocenter on the back-direction edge of the fault when the station is in the backward direction, if $m_5 = 0$. This can be circumvented by the use of the back-direction isochrone velocity ratio $\tilde{c}_b'$ from (10). We define

$$c_2^*(\mathbf{x}_s) \;:=\; \tilde{c}_b' + m_5(\tilde{c}' - c_b') \tag{13}$$

$c_2^*(\mathbf{x}_s)$ is very similar to $c_1{}^*$, except for having a more appropriate value for stations located in a position where there is almost no component of rupture toward them. However, a third version is also possible using back-direction isochrone velocity ratio $\tilde{c}_b'$ as a floor under $m_5\,\tilde{c}'$:

$$c_3^*(\mathbf{x}_s) := \max(m_5\tilde{c}', \tilde{c}_b') \tag{14}$$

Preliminary results indicate that c_3^* works a bit better than c_2^* because m_5 is rarely very small for most geometries, meaning that the back-direction isochrone velocity ratio influences $c_2^*(\mathbf{x}_s)$ too much.

Polarization of Ground Motion and Radiation Patterns

A problem with c^* is that it does not account for the polarization of ground motion or the closely related radiation pattern. We have tried to develop a simple approximation of the radiation pattern of a finite source. Typically, developers of ground motion prediction relations have available to them information on only two points on a finite fault, the hypocenter and the point on the fault closest to a particular station. Thus, we have concentrated on developing from only these two points an approximate radiation pattern for a finite fault. Our approximation works reasonably well, as will be shown below, but has limitations that might be removed through consideration of other points on the fault surface.

Point Source Radiation Patterns

We start with the radiation pattern of a point source. In Appendix A equations A12-A19, we have derived (relatively) simple expressions for the far-field S wave radiation patterns. We have made the following assumptions:

Assumptions:

1. The S wave leaves any point $\mathbf{x}$ on the fault going straight to the station
2. The S wave is vertically incident on the station

This means that the free surface amplification is 2 for both components of the S wave, and that the S wave has no vertical component. This latter restriction can be removed if necessary. We account for the radiation pattern as follows. Let u be distance along strike and v be distance down dip from the origin of coordinates on the rectangular slipped area of the fault (Figure 3), and let d_o be the depth to the origin of the (u,v,w) coordinate system, i.e. d_o is depth to the top of the slipped zone. Let $\hat{\mathbf{z}}$ point upward. Then a point $\mathbf{x}$ on the fault has coordinates $\mathbf{x} = (u,v,0)$. The far-field S radiation pattern for the u-component (fault parallel, FP) of motion at station location $\mathbf{x}_s$ for slip at $\mathbf{x}$ is $\mathcal{R}_u(\mathbf{x}_s,\mathbf{x})$. The fault-normal (FN, transverse) unit vector is $\hat{\mathbf{t}} = -(\hat{\mathbf{u}} \times -\hat{\mathbf{z}})$, which lies in the horizontal plane, Figure 3, and the radiation pattern term for transverse motion is $\mathcal{R}_t(\mathbf{x}_s,\mathbf{x})$. We use the $\hat{\mathbf{t}}$ unit vector to explicitly differentiate it from the unit-vector normal to the (possibly dipping) fault, $\hat{\mathbf{w}}$ (see Figure 4). These radiation pattern terms have both positive and negative lobes, so it will be necessary to use their absolute values in practice, as will be shown later. Note that these radiation patterns, derived in Appendix A, are for FP and FN motions at the station, not the usual SV and SH radiation patterns.

These radiation patterns also have sharp nodes with zero amplitudes, which are both unrealistic and problematic when the logarithm is taken. We expect that nodes will be progressively blurred by scattering as the S wave propagates farther, and the amount of blurring probably scales with the path length measured in numbers of wavelengths. Also, for stations very near the fault trace, channeling of waves in a fault-zone low-velocity-zone may blur radiation patterns. Because directivity is also a form of radiation pattern, the same blurring should occur to it, although some of the blurring of directivity might result from heterogeneous rupture behavior on the fault.

However, to blur the radiation patterns shown in this report, we use an ad-hoc waterlevel ε, set to some arbitrary reasonable value, and we take the absolute value of the radiation pattern:

$$\mathcal{R}'_p(\mathbf{x}_s,\mathbf{x}) := \max\left(\left|\mathcal{R}_p(\mathbf{x}_s,\mathbf{x})\right|, \varepsilon\right), \quad p = u \text{ or } t,\ 0 < \varepsilon \approx 0.2 \tag{15}$$

Because the synthetic simulations have perfect radiations patterns, we use $\varepsilon = 0.01$ when comparing with simulated data. For real data $\varepsilon \approx 0.2$ might be better. Attenuation relation developers might need to make ε an empirically determined function of period (Pitarka *et al.*, 2000). While we also expect that the radiation pattern maxima will be blurred and reduced by scattering (perhaps by a factor of 2?), we currently only blur the nodes because $\ln(1) - \ln(0.5)$ is much less than $\ln(\varepsilon) - \ln(0)$.

Finite Source Radiation Patterns

Because the source area is not actually a point, it is necessary to modify the radiation pattern to account for source finiteness. In this analysis we consider two points, $\mathbf{x}_h$ and $\mathbf{x}_c$. For very long period motions we might expect S waves from $\mathbf{x}_h$ and $\mathbf{x}_c$ to interfere constructively (i.e. with phase coherence), but for short periods they would not. In the forward directivity region coherent summation is expected, whereas in the other directions the arrival times from the hypocenter and closest point will be well separated, leading to phase incoherence. Stations in the forward directivity region will probably see similar radiation patterns from the two points, whereas most other points will not. Thus, in general incoherent summation will prevail, and when it does not, in the forward direction, the radiation patterns (as seen at the station) will be similar. Coherent summation would be $\mathcal{R}_p(\mathbf{x}_s,\mathbf{x}_h) + \mathcal{R}_p(\mathbf{x}_s,\mathbf{x}_c)$.

In this report we approximate the finite fault radiation pattern by the average of the radiation patterns of the hypocenter and the closest point:

$$\overline{\mathcal{R}}_p(\mathbf{x}_s,\mathbf{x}_c,\mathbf{x}_h) := \frac{1}{2}\mathcal{R}'_p(\mathbf{x}_s,\mathbf{x}_h) + \frac{1}{2}\mathcal{R}'_p(\mathbf{x}_s,\mathbf{x}_c), \quad p = t \text{ or } u. \tag{16}$$

Even though distance to the hypocenter r_h can be much greater than rupture distance r_r, we choose not to downweight $\mathcal{R}_p(\mathbf{x}_s,\mathbf{x}_h)$ too much because the radiation at the station will be dominated by the region between the hypocenter and closest point; in fact, since a station within the slipped zone of the fault, like station 2 in Figure 2, is normal to the closest point, such a station is on a node of $\mathcal{R}_t(\mathbf{x}_s,\mathbf{x}_c)$ (transverse motion), which is clearly inappropriate for stations close to a fault. This is a drawback of our need to use only information about the hypocenter and closest point. For such a station the fault-normal (transverse) motion is provided by the radiation pattern from the hypocenter. An advantage of our averaging formulation is that most stations will have no nodes.

When comparing to observed geometric mean horizontal data it is necessary to use the geometric average radiation pattern, which in this report is defined as

$\overline{\mathcal{R}}_{ga} := \sqrt{\overline{\mathcal{R}}_u \overline{\mathcal{R}}_t}$.

There are a number of problems involved in using the geometric average of highly polarized pulses, which will be discussed later.

Recommended Predictor Variables

We define a "source anisotropy factor" to be any combination of radiation patterns and directivity. A source anisotropy factor has the form

$$A^p \quad := \quad (\text{some form of } \tilde{c}')(\text{some form of } \mathcal{R}_p)$$

where p is the component of ground motion (u or t), and some form of blurring of radiation pattern nodes is employed. In all cases, the predictor variable is A^p**.**

For use in empirical regression relations, we want to have predictors and a functional form for directivity, polarization, and radiation pattern that are capable of capturing their dependence on magnitude, distance, and period. Typically, ground motions y could be fit by a form like

$$\ln(y) = f(M,r_r,T) + k_2(M,r_r,T)\ln(A^p) \qquad (17)$$

where $f(M,r_r,T)$ is the non-directive part of the model and $k_2\left(M,r_r,T\right)$ is an empirically determined coefficient that may vary with magnitude *M*, distance r_r, and period *T*. We will show several possible definitions of A^p. Although it might be possible to develop functional forms for which the dependence on *T* is not needed, it is not done here.

Possible predictor variables are:

$$A_1^p := \quad m_5\,\tilde{c}'\,\overline{\mathcal{R}}_p, \quad p = u \text{ or } t \qquad (18)$$

This is very simple, but has the disadvantage that m_5 can be very close to zero. A preferable remedy is to put a floor under $m_5\,\tilde{c}'$ by using c_3^*:

$$A_2^p := \quad \max\left(m_5\tilde{c}', \tilde{c}_b'\right)\overline{\mathcal{R}}_p = c_3^*\,\overline{\mathcal{R}}_p, \quad p = u \text{ or } t, \qquad (19)$$

where $\tilde{c}_b' = 0.4444$ for $v_r/\beta = 0.8$. This covers the unusual but possible case that m_5 is very small.

In the above we have concentrated on using only isochrone velocity to characterize the effect of a finite source, but equation A3 shows that the length of the line integral $\oint\limits_{\mathbf{x}(t,\mathbf{x}_s)} dl$ also is a finite source effect contributing to the ground motion.

Comparisons (shown later) indicate that the effect of the line integral might be simulated by including *D* in the predictor variables:

$$A_3^p := \quad D\,\tilde{c}'\,\overline{\mathcal{R}}_p, \quad p = u \text{ or } t, \qquad (20)$$

or

$$A_4^p := \quad D\,m_5\tilde{c}'\,\overline{\mathcal{R}}_p, \quad p = u \text{ or } t \qquad (21)$$

or the preferred

$$A_5^p := \quad D\,\max\left(m_5\tilde{c}', \tilde{c}_b'\right)\overline{\mathcal{R}}_p = D\,c_3^*\,\overline{\mathcal{R}}_p, \quad p = u \text{ or } t. \qquad (22)$$

Of the batch listed above, we recommend $\ln(A_2^p)$ and $\ln(A_5^p)$. However, note that it is possible for D to equal zero, so in practice some sort of floor should be put under D. We have not yet derived a theoretically justified value of this floor.

Handling Multiple-Segment Faults

The above formulation of isochrone directivity based on $\tilde{c}'$ does not generalize easily to handle multiple fault segments. We have developed a formulation for sources consisting of multiple fault planes (Figure 5), in which we effectively flatten the fault. The proposed approach is similar to the generalization of the Somerville et al. (1997) directivity parameters to multiplanar faults proposed by J. Boatwright (personal communication). Our formulation is simple but it can introduce spatial discontinuities into the source anisotropy factors as a function of station position.

$\tilde{c}'$ for a Single Segment

On the i-th planar segment let $\mathbf{x}_c^i$ be the point closest to the station. On all segments draw a horizontal line at the same downdip coordinate v_h as the hypocenter (see Figure 5). Define the pseudo-hypocenter $\mathbf{x}_h^i$ of the i-th planar segment to be the point on the horizontal line closest to the true hypocenter $\mathbf{x}_h$. For one of the segments (nominally taken as segment H) the pseudo-hypocenter will coincide with the true hypocenter. Define the rupture distance of the i-th segment to be $r_r^i = \left|\mathbf{x}_c^i - \mathbf{x}_s\right|$ and the hypocentral distance of the i-th segment to be $r_h^i = \left|\mathbf{x}_h^i - \mathbf{x}_s\right|$. Of course, $r_r = \min\limits_i (r_r^i)$ and $\mathbf{x}_c = \min\limits_i (\mathbf{x}_c^i)$. Define $D_i = \left|\mathbf{x}_c^i - \mathbf{x}_h^i\right|$. Then the approximate isochrone velocity ratio of the i-th segment is

$$\tilde{c}_i' := \left(\frac{\beta}{v_r} + D_i^{-1} \left(r_r^i - r_h^i \right) \right)^{-1}, \quad D_i > 0. \tag{23a}$$

$$= \frac{v_r}{\beta}, \quad D_i = 0. \tag{23b}$$

This is the same form as equation (9) for a single segment fault. Similarly, we can let m_5^i be m_5 for the i-th segment. (If the segment containing the true hypocenter is segment H, then only m_5^H is different from unity.) The average radiation pattern of the i-th segment is defined to be $\overline{\mathcal{R}}_p^i = \overline{\mathcal{R}}_p\left(\mathbf{x}_s, \mathbf{x}_c^i, \mathbf{x}_h^i\right), \quad p =$ desired direction. Note, however, that for multi-segment faults FN and FP are not unique, and the average radiation patterns may need to be rotated into some desired direction. In Appendix A the expression A13 is valid for any horizontal polarization direction $\hat{\mathbf{p}}$, but subsequent expressions are specialized to $\hat{\mathbf{p}}$ being $\hat{\mathbf{t}}$, fault-normal, or $\hat{\mathbf{u}}$, fault-parallel, for a single segment. In the following we will define $\hat{\mathbf{u}}^i$ and $\hat{\mathbf{t}}^i$ to be fault-parallel and fault-normal directions, respectively, for the i-th segment.

Flattening the Fault

Consider a fault consisting of N planar segments, as in Figure 5, where we assume that the $i = H$ segment contains the true hypocenter, the *L*-th segment is the closest to the station, and segments *H*+1 through *L*-1 are between segments *H* and *L* in space. The multi-segment generalization of *D* is

$$D^* := \sqrt{\left(\sum_{i=1}^{N} s_i \right)^2 + d_L^2} \tag{24}$$

Lengths s_i are shown in Figure 5 and defined as follows: If point **x** on the fault has coordinates (*u, v, 0*), as in Figure 3, then $s_i = \left| u_c^i - u_h^i \right|$. Then an overall approximate isochrone velocity ratio for the multi-segment fault can be defined as

$$\tilde{c}' = \left(\frac{\beta}{v_r} + \left(D^*\right)^{-1}\left(r_r - r_h\right)\right)^{-1}, \quad D^* > 0. \tag{25a}$$

$$= \frac{v_r}{\beta}, \quad D^* = 0. \tag{25b}$$

For simple geometries like that in Figure 5a the above algorithm for selecting pseudohypocenters $\mathbf{x}_h^i$ and closest points $\mathbf{x}_c^i$ approximates the likely path of rupture fairly well. However, for fault networks that have many long cross-cutting faults or several parallel fault strands, the line segments connecting $\mathbf{x}_h^i$ and $\mathbf{x}_c^i$ can lead to a D^* that is much longer than the actual length of rupture, and consequently $\tilde{c}'$ calculated using (25a) can exceed 4.0. If so, we replace that $\tilde{c}'$ with the following:

$$\tilde{c}' = \left(\frac{\beta}{v_r} + D^{-1}\left(r_r - r_h\right)\right)^{-1}, \quad D > 0 \tag{25c}$$

where $D = \left|\mathbf{x}_c - \mathbf{x}_h\right|$ is the straight-line distance from the hypocenter to the closest point.

To develop the multi-segment source anisotropy terms we must include radiation patterns. In this formulation we will ignore the fact that the segments are not parallel to each other, i.e. $\hat{\mathbf{u}}^H \neq \hat{\mathbf{u}}^L$ and $\hat{\mathbf{t}}^H \neq \hat{\mathbf{t}}^L$. We define "effective" fault-parallel and fault-normal radiation patterns

$$\overline{\mathcal{R}}_{FP}\left(\mathbf{x}_s, \mathbf{x}_c, \mathbf{x}_h\right) := \frac{1}{2}\mathcal{R}'_{\hat{\mathbf{u}}^H}\left(\mathbf{x}_s, \mathbf{x}_h\right) + \frac{1}{2}\mathcal{R}'_{\hat{\mathbf{u}}^L}\left(\mathbf{x}_s, \mathbf{x}_c\right) \tag{26a}$$

$$\overline{\mathcal{R}}_{FN}\left(\mathbf{x}_s, \mathbf{x}_c, \mathbf{x}_h\right) := \frac{1}{2}\mathcal{R}'_{\hat{\mathbf{t}}^H}\left(\mathbf{x}_s, \mathbf{x}_h\right) + \frac{1}{2}\mathcal{R}'_{\hat{\mathbf{t}}^L}\left(\mathbf{x}_s, \mathbf{x}_c\right) \tag{26b}$$

where we recall that $\mathbf{x}_h \equiv \mathbf{x}_h^H$ and $\mathbf{x}_c \equiv \mathbf{x}_c^L$. Here we are not bothering to rotate the radiation pattern terms into a common orientation. For fault segments whose strikes differ by less than 30° this approximation is probably not too bad.

Using this formulation for multiple segment faults, we define a preferred source anisotropy factor analogous to single segment equation (19):

$$A_2^p := \max\left(m_5^L \tilde{c}', \tilde{c}'_b\right)\overline{\mathcal{R}}_p, \quad p = FN \text{ or } FP, \tag{27}$$

where in practice m_5^L will have the value unity except when $L=H$ (recall, L is not the number of segments, but rather the index of the segment containing the closest point to the station), $\tilde{c}'$ is from (25), $\overline{\mathcal{R}}_p$ is from (26), and $\tilde{c}'_b$ is from (10). The second preferred source anisotropy factor, analogous to single segment equation (22) is

$$A_5^p := D^* \max\left(m_5^L \tilde{c}', \tilde{c}'_b\right) \overline{\mathcal{R}}_p, \quad p = FN \text{ or } F\text{P}. \tag{28}$$

This formulation of source anisotropy factors for multi-segment faults (equations 27 and 28) has the advantage that it is quite simple. It has two disadvantages. First, the exact fault-normal and fault-parallel directions are not defined. Second, these source anisotropy factors can be spatially discontinuous. As the station is moved, D^* and the average radiation pattern can change discontinuously as the closest point $\mathbf{x}_c$ jumps from one segment to another.

Our expression (25) for $\tilde{c}'$ gives an intuitively satisfying result, but our expression (26b) for the fault-normal component of radiation pattern $\overline{\mathcal{R}}_{FN}$ is not so satisfying. Figure 6 shows these terms calculated for a multisegment approximation of the fault rupture of the 1992 Landers, California, earthquake. $\tilde{c}'$ is peaked along the curving fault trace, as desired. There are some discontinuities in $\tilde{c}'$ caused by the closest point moving across a segment boundary, but these discontinuities are not very strong. On the other hand, the map of $\ln\left(\overline{\mathcal{R}}_{FN}\right)$ is not so satisfying. It shows strong fault-normal motion is expected off the ends of the fault, but not along the fault trace itself. This is caused by the breakdown of the approximation of the finite fault radiation pattern by a sum of the radiation patterns from the hypocenter and the closest point (equation 26). For a planar fault the hypocentral radiation pattern provides the fault-normal motion along the fault trace (which is the pink wedge along $X = 0$, $Y > 0$, in Figure 6. However, the curving fault bends away from this radiation pattern lobe and the radiation pattern term from the closest point does not provide the needed fault-normal motion. Consequently, a better approximation of the finite-fault radiation pattern is needed.

COMPARISONS WITH 1D SIMULATIONS

To determine whether the proposed predictor variables might possibly be useful, we compared the predictions to synthetic ground motions calculated for a variety of earthquake source models and station distributions in a vertically varying ("1D") geologic structure. These problem geometries were defined by Abrahamson (2003). We calculated these synthetic motions using a hybrid broadband simulation procedure that combines a stochastic approach at high frequencies with a deterministic approach at low frequencies (Graves and Pitarka, 2004). A kinematic description of fault rupture is used, incorporating spatial heterogeneity in slip, rupture velocity and rise time by discretizing an extended finite-fault into a number of smaller subfaults. The stochastic approach sums the response for each subfault assuming a random phase, an omega-squared source spectrum and generic Green's functions (Boore, 1983). Gross impedance effects are incorporated using quarter wavelength theory (Boore and Joyner, 1997). The deterministic approach sums the response for many point sources distributed across each subfault, with theoretical Green's functions calculated using a 1D frequency-wavenumber integration algorithm.

In this report we consider four different rupture models or events, SA (the only strike slip event), and reverse events RB, RG, and RK (Table 1). For each event (source geometry) 24 simulations of ground motions were calculated for all stations. The 24 simulations consisted of 12 different hypocenter locations equally spaced in the northern half of the fault and two types of slip distributions, shallow and deep. Each combination of event and realization was given a code, e.g. RG24 for the 24th realization of event (source geometry) RG.

Table 1. Rupture Dimensions for Source Models in 1D Simulations

Event Name	Mag	Area (km^2)	W (km)	L (km)	Dip	Top of Rupture (km)
SA	6.5	325	13	25	90	0
RB	6.5	324	18	18	45	0
RG	7.0	1008	28	36	45	0
RK	7.5	3164	28	113	45	0

We used as "data" y_i either the simulated fault-normal (FN) or fault-parallel (FP) response spectral accelerations at 3 s period and 5% damping, or the geometric average of the FN and FP spectral accelerations . For each event the data from all realizations were lumped together and were fitted with a simple non-directive model:

$$\ln(y_i) = C1(T) + C2(T)\ln\left(r_{r_i} + C3(T)\right) + \rho_i$$

where y_i was either the FN, FP, or geometric mean of the FN and FP spectral acceleration at period $T = 3$ s at station *i*, and r_{r_i} is the closest distance (rupture distance) to the fault from station *i*. Unknown coefficients *C1* and *C2* vary from realization to realization; *C3* is common to all realizations, and ρ_i is the residual between data and fitted non-directive model. A separate non-directive model was developed for each component of motion (FN, FP, and GA). Data at all distances were used, but in the following plots only residuals for $r_{r_i} < 100$ km are shown.

We anticipate that directivity effects will be handled in ground motion prediction relations as a correction to the non-directive part of the relationship, in a manner similar to $X\cos(\theta)$ of Somerville et al. (1997). Therefore, we first fit the synthetic ground motion to the above simple model and then we examine the residuals ρ_i for directivity effects.

Rather than quantify the effects, our goal here is to demonstrate that the candidate predictors discussed above have the capability to explain a significant part of the scatter in the residuals ρ_i. We anticipate a linear relationship in the logarithmic scale because isochrone theory predicts that the ground motion amplitude should be a linear function of isochrone velocity or the length of the isochrones or their product. If such a linear relationship is observed in our limited simulated data set, there is some hope that the correlation will persist when applied to a broader data set of real data containing a wider range of sources. It might be argued that a nonlinear relationship would be acceptable, but such a relationship would not be predicted by theory and could not be expected to persist when applied to a data set different from the synthetic data used here. In fact, in the course of this work we have seen examples of nonlinear relationships with the logarithms of candidate predictor variables at small and large magnitudes, but the nonlinear functions that worked for the small magnitude events were quite different from those that worked for large events.

Now we show preliminary results for two of the candidate predictor variables listed above, namely

$$\ln(A_1^p) = \ln(m_5\, \tilde{c}'\, \overline{\mathcal{R}}_p), \quad p = u(FP) \text{ or } t(FN) \text{ or GA}$$

and

$$\ln(A_3^p) = \ln(D\, \tilde{c}'\, \overline{\mathcal{R}}_p), \quad p = u(FP) \text{ or } t(FN) \text{ or GA}.$$

For the former predictor an early now-disfavored version of the m_5 algorithm was used, in which it was not required that the closest point be on the edge of the fault for non-unity m_5. This old version of the m_5 algorithm only differs from the new one at stations that are nearly perpendicular from the hypocenter. The latter predictor is interesting because it includes the factor D. Neither of these predictor variables is currently favored because they put no floor under D or m_5, but they illustrate the basic aspects of the comparisons. When calculating the predictor variables, a water level $\varepsilon = 0.01$ was used because the synthetics have perfect radiation pattern nodes.

Event SA Analysis

Figure 7 shows maps of the geometric average, fault normal, and fault parallel residuals ρ_i for SA02, strike-slip event SA, M 6.5, hypocenter realization 02. This fault extends from Y=12.5 to Y = -12.5 km. As the hypocenter in this (and all other) realization is in the "north" (+Y end of the fault), the directivity is apparent in the generally large positive residuals (with respect to a non-directive model) in the "south" (-Y) end of the fault.

This example points out possible problems in the use of the geometric average motion when the ground motions are strongly polarized by directivity and radiation patterns. The effect of radiation pattern can be seen in Figure 8, which is Figure 7 with probable ground motion polarization directions superposed in green. The big FN pulse is shown by FN residuals along strike in the south end of the fault (X=0, Y=120) being large and positive whereas the FP residuals are large and negative at that point. A similar effect is seen at X=80, Y=0, where a large FP motion is observed. In both of these locations one component of motion is quite small, dragging down the geometric average (Figure 9). However, at X=60, Y=60 the motion is dominated by SV (radial) motion, so the geometric average is not depressed so much. This is an example of the geometric average motion being affected by the choice of coordinate system. Figure 10 shows a similar pattern for a different hypocenter location in event SA.

Figure 11 shows the correlation of the residuals for geometric average motion compared with two different predictor variables, A_1^p and A_3^p (using the early m_5 algorithm). The correlations are shown as scatter plots using residuals for all realizations of event SA, and the two predictor variables and the residuals are shown as maps for two specific realizations, SA02 and SA04. The general agreement of the maps indicates that the isochrone directivity factors capture much of the directivity in the simulations, although there is considerable scatter and nonlinearity in the scatter plots of residuals (upper panel).

Figure 12 shows that the FN and FP residuals show a stronger correlation with the predictors than do the GM residuals. Also, the FN residuals show a smaller scatter than the GM. This is another indication that reliance on the geometric average motion of highly polarized pulses can be problematic. Generally the FN and FP residuals are fairly linearly related to the both predictors, but the upper right panel shows that for FP motion the A_1^p predictor tends to overpredict FP motion. This tends to happen close to the fault, where the synthetic motion is smaller than the prediction. This discrepancy might be related to an inappropriate value for the radiation pattern.

Reverse Fault Analyses - Events RB, RG, and RK

Figures 13 through 18 show the same general patterns for events RB (M6.5), RG (M 7.0), and RK (M 7.5). The spatial maps of the geometric average residuals resemble the maps of the predictors, and the residuals correlate with the predictors better for FN and FP components of motion than for the geometric average component of motion. In general, the predictors work better for the smaller events than for the larger events. This is probably because the approximation of the finite source radiation pattern by two points sources is more accurate for the smaller events. For a very large event the hypocenter can be 100 km from the station, whereas the closest point on the fault can be only a few km distant, so an equal weighting of the two might not be very appropriate. A better solution might be to use the radiation pattern of the point between the hypocenter and the closest point that radiates the strongest motion at the station.

CONCLUSIONS

We have suggested 5 different predictor variables, with the recommended predictor variables being A_2^p and A_5^p.

Developers of ground motion prediction relations will probably need to make radiation pattern water level ε an empirically determined function of period. Certainly following us and using $\varepsilon = 0.01$ with real data will be wrong. We cannot determine the proper number from the synthetic data.

Developers might want to experiment (cautiously) with the ratio v_r/β, but $v_r/\beta = 0.8$ is probably acceptable.

Our directivity measures currently do not compensate for the fact that slip tapers toward the edges of all fault. This suggests that a new distance measure is needed, similar to Campbell's seismogenic distance, which excludes the low-slip-amplitude peripheries of faults.

The use of geometric mean motions for polarized pulses can be problematic. The main problem is that the geometric mean is strongly controlled by the smaller component, and the amplitude of motion on the smaller component is controlled by random factors in the Earth that are not present in any models. Thus, the geometric average can have a large component of uncertainty.

APPENDIX A. EQUATIONS FOR THE RADIATION PATTERN

The following discussion uses the basic notation and geometry of Spudich and Frazer (1984), the erratum Spudich and Frazer (1987), and Spudich and Xu (2003). Please see those paper for the definitions of terms not defined here. In the following we use SF to mean Spudich and Frazer (1984) and we use SF*nn* to refer to equation *nn* from SF.

The simplest form of isochrone theory assumes that the space- and time-dependence of the earthquake slip time-function $\mathbf{d}(\mathbf{x},t)$ can be separated,

$$\mathbf{d}(\mathbf{x},t) = \mathbf{s}(\mathbf{x}) f[t - t_r(\mathbf{x})]. \tag{A1}$$

Here bold characters denote vectors, $\mathbf{x}$ is a point on the fault, $\mathbf{s}(\mathbf{x})$ is the amplitude of the slip as a function of position on the fault, and the slip time function $f[t - t_r(\mathbf{x})]$ is normalized to unit final amplitude, i.e. $f(\infty) = 1$. The time behavior $f(t)$ is the same everywhere on the fault – in other words in this simple model the rise time of slip is constant everywhere on the fault, but the initiation time (or rupture time) $t_r(\mathbf{x})$ and the slip amplitude $\mathbf{s}(\mathbf{x})$ vary over the fault surface. This is a simple but not unrealistic model for a slip time function in a real earthquake (e.g. Heaton, 1990). The time derivative of $f(t)$ is $\dot{f}(t)$.

Using (A1) the displacement in the direction of an arbitrarily oriented unit vector $\hat{\mathbf{p}}$ at the station $\mathbf{x}_s$, given by SF10, can be written with the slip time-function factored out,

$$\hat{\mathbf{p}} \cdot \mathbf{u}^w(\mathbf{x}_s,t) = u_p^w(\mathbf{x}_s,t) = \dot{f}(t) * I_p^w(\mathbf{x}_s,t), \qquad \text{(A2)}$$

where w = P for P waves and S for S waves and where

$$I_p^w(\mathbf{x}_s,t) := \oint_{\mathbf{x}(t,\mathbf{x}_s)} \mathbf{s}(\mathbf{x}) \cdot \mathbf{G}_p^w(\mathbf{x},\mathbf{x}_s) c(\mathbf{x},\mathbf{x}_s) dl, \qquad \text{(A3)}$$

with the path of integration $\mathbf{x}(t,\mathbf{x}_s)$ being the isochrone for time t (defined in SF9). Henceforth for simplicity we will write these path integrals without the isochrone specifically listed. Isochrones for a specific example are shown in Figure 1d. The color field in that figure shows the real part of the integrand of (A3).

Although equation (A3) is the basic isochrone integral, Spudich and Xu (2003) have rearranged terms so that the dependence on the direction (polarization) of ground motion $\hat{\mathbf{p}}$ is factored out of the integrand to the greatest extent possible. Let $\hat{\mathbf{u}}$ and $\hat{\mathbf{v}}$ be unit vectors lying in the fault plane, with $\hat{\mathbf{u}}$ being horizontal and being directed along strike and with $\hat{\mathbf{v}}$ pointing downdip. Define unit vector $\hat{\mathbf{w}} = \hat{\mathbf{u}} \times \hat{\mathbf{v}}$ as the normal to the fault, which is different from the typical engineering use of the term 'fault normal' (Figure 3). The slip vector is $\mathbf{s} = s_u \hat{\mathbf{u}} + s_v \hat{\mathbf{v}}$. Also shown in Figure 3 are the $\hat{\mathbf{t}}$ unit vector, which is perpendicular to the fault in the horizontal plane, (typically called 'fault-normal' or 'strike-normal' in engineering; we also call this direction 'transverse' here), and the $\hat{\mathbf{z}}$ unit vector, pointing vertically upward. Typically we will evaluate all the expressions for components of motion $\hat{\mathbf{p}} = \hat{\mathbf{u}}, \hat{\mathbf{t}},$ or $\hat{\mathbf{z}}$, as these tend to be the dominant polarization directions of near-fault motions.

Then, from equation (18) in Spudich and Xu (2003) we have that the S wave ground motion $\mathbf{u}^S$ in the $\hat{\mathbf{p}}$ direction at the station $\mathbf{x}_s$ is

$$\hat{\mathbf{p}} \cdot \mathbf{u}^S = \dot{f}(t) * \oint \mu Q \, \mathbf{s} \cdot [F_p^S(\hat{\mathbf{p}} \cdot \hat{\mathbf{b}}_0)\mathbf{X}_1 + F^c(\hat{\mathbf{p}} \cdot \hat{\mathbf{c}}_0)\mathbf{X}_2] \, c \, dl. \qquad \text{(A4)}$$

Here the SH free surface coefficient is F_c and the complex SV free surface coefficient is F_p^S where $p = u, t,$ or z is the component of motion. Vectors $\hat{\mathbf{r}}$, $\hat{\mathbf{b}}$, and $\hat{\mathbf{c}}$ are the directions of particle motions for P, SV and SH waves, respectively, shown in Figure 4. Note that at the station $\mathbf{x}_s$ the P wave is polarized in direction $\hat{\mathbf{r}}_o$, the SV wave is polarized in the $\hat{\mathbf{b}}_0$ direction, and the SH wave is polarized in direction $\hat{\mathbf{c}}_0$. $\mathbf{X}_1$ contains most of the radiation pattern for SV and $\mathbf{X}_2$ contains most of the radiation pattern for SH. They are given by SF as

$$\mathbf{X}_1 = (\hat{\mathbf{n}} \cdot \hat{\mathbf{r}})\hat{\mathbf{b}} + (\hat{\mathbf{n}} \cdot \hat{\mathbf{b}})\hat{\mathbf{r}} \tag{A5}$$

and

$$\mathbf{X}_2 = (\hat{\mathbf{n}} \cdot \hat{\mathbf{r}})\hat{\mathbf{c}} + (\hat{\mathbf{n}} \cdot \hat{\mathbf{c}})\hat{\mathbf{r}}\,. \tag{A6}$$

The geometric spreading factor $S = [|dA/d\Omega|]^{1/2}$ and the ratio of impedences at the two ends of the S ray are contained in the term

$$Q := [4\pi\ S(\mathbf{x}_s,\mathbf{x})]^{-1}[\rho_0\rho\beta_0\beta^5]^{-1/2}$$

where the subscript "0" denotes a material property at $\mathbf{x}_s$ and lack of a subscript denotes a property at the fault.

Approximations for Engineering Use

- A1: no laterally heterogeneous structure.
- A2: $\hat{\mathbf{r}}$, $\hat{\mathbf{b}}$, and $\hat{\mathbf{c}}$ calculated assuming straight rays (Figure 4)
- A3: $\hat{\mathbf{r}}_o$, $\hat{\mathbf{b}}_o$, and $\hat{\mathbf{c}}_o$ calculated ***assuming the ray is vertical at the station***, i.e. $\hat{\mathbf{r}}_o = -\hat{\mathbf{z}}$, $\hat{\mathbf{b}}_o =$ [illegible]$_o$, and $\hat{\mathbf{c}}_o =$ [illegible]$_o$. This means that $\hat{\mathbf{z}} \cdot \hat{\mathbf{b}}_o = \hat{\mathbf{z}} \cdot \hat{\mathbf{c}}_o = 0$, i.e. the ***S wave has no vertical component.*** This also implies that $F_p^s = F^c = 2$, the free surface coefficient is the SH component for both horizontal components of motion.

With these approximations the *p*-component of S-wave displacement is

$$\begin{aligned}\hat{\mathbf{p}} \cdot \mathbf{u}^s &= \dot{f}(t) * \oint 2\mu\, Q\, \mathbf{s} \cdot [(\hat{\mathbf{p}} \cdot \hat{\mathbf{b}}_0)\mathbf{X}_1 + (\hat{\mathbf{p}} \cdot \hat{\mathbf{c}}_0)\mathbf{X}_2]\, c\ dl \\ &= \dot{f}(t) * \oint 2\mu\, Q \Gamma_p\ c\ dl \end{aligned} \tag{A7}$$

$$\text{where } \Gamma_p = \mathbf{s} \cdot [(\hat{\mathbf{p}} \cdot \hat{\mathbf{b}}_0)\mathbf{X}_1 + (\hat{\mathbf{p}} \cdot \hat{\mathbf{c}}_0)\mathbf{X}_2] \tag{A8}$$

Isochrone velocity ratio

Isochrone velocity is given in units of speed, and it seems appropriate to normalize by the local shear wave velocity because the Ben-Menahem directivity factor is a function of the ratio of the rupture velocity to the local shear wave velocity. For that reason, we define an *isochrone velocity ratio* to be the ratio of isochrone velocity and shear wave velocity,

$$c' := c/\beta \tag{A9}$$

Using this, the p-component of S-wave displacement becomes

$$\hat{\mathbf{p}}\cdot\mathbf{u}^S = \dot{f}(t) * \int 2\mu\, Q'\, \mathbf{s}\cdot[(\hat{\mathbf{p}}\cdot\hat{\mathbf{b}}_0)\mathbf{X}_1 + (\hat{\mathbf{p}}\cdot\hat{\mathbf{c}}_0)\mathbf{X}_2]\, c'\, dl \tag{A10}$$

where $Q' := [4\pi\, S(\mathbf{x}_s,\mathbf{x})]^{-1}[\rho_0\rho\beta_0\beta^3]^{-1/2}$. (A11)

Radiation pattern definition

Define radiation pattern for the p-component of motion:

$$\mathcal{R}_p = \hat{\mathbf{s}}\cdot[(\hat{\mathbf{p}}\cdot\hat{\mathbf{b}}_0)\mathbf{X}_1 + (\hat{\mathbf{p}}\cdot\hat{\mathbf{c}}_0)\mathbf{X}_2] \tag{A12}$$

where $\hat{\mathbf{s}}$ is a unit vector in the direction of slip, which implies that $\Gamma_p = |\mathbf{s}|\mathcal{R}_p$.

To evaluate the radiation pattern, we need to define the fault geometry and coordinate system. Let u, v, and w be coordinates in the fault plane, following unit vectors $\hat{\mathbf{u}}, \hat{\mathbf{v}},$ and $\hat{\mathbf{w}}$, with $\mathbf{x} = (u,v,w)$.
Then the hypocenter is at $\mathbf{x}_h = (u_h,v_h,w_h)$ and the station is at $\mathbf{x}_s = (u_s,v_s,w_s)$. Let the point in the slipped rectangle closest to $\mathbf{x}_s$ be $\mathbf{x}_c = (u_c,v_c,0)$. Then the S wave radiation pattern for the p-component of motion can be written

$$\mathcal{R}_p(\mathbf{x}_s,\mathbf{x}) = (\hat{\mathbf{p}}\cdot\hat{\mathbf{b}}_0)\Big[(\hat{\mathbf{n}}\cdot\hat{\mathbf{r}})(\hat{\mathbf{s}}\cdot\hat{\mathbf{b}}) + (\hat{\mathbf{n}}\cdot\hat{\mathbf{b}})(\hat{\mathbf{s}}\cdot\hat{\mathbf{r}})\Big] + (\hat{\mathbf{p}}\cdot\hat{\mathbf{c}}_0)\big[(\hat{\mathbf{n}}\cdot\hat{\mathbf{r}})(\hat{\mathbf{s}}\cdot\hat{\mathbf{c}}) + (\hat{\mathbf{n}}\cdot\hat{\mathbf{c}})(\hat{\mathbf{s}}\cdot\hat{\mathbf{r}})\big] \tag{A13}$$

This is the most useful expression for the radiation pattern. All the dot products in this daunting term can easily be evaluated using geometric information typically available, as given in the following equations. In the following we use the notation $s\delta$ and $c\delta$ to mean $\sin(\delta)$ and $\cos(\delta)$, respectively. We will evaluate the radiation pattern for the strike-parallel ($\hat{\mathbf{u}}$)and the strike-normal ($\hat{\mathbf{t}}$) components of S-wave motion. Note that dip δ and rake $\lambda$are given parameters, so terms like $s\delta$ and $c\delta$ $(\sin(\delta)$ and $\cos(\delta))$ and $s\lambda$ and $c\lambda$ $(\sin(\lambda)$ and $\cos(\lambda))$ are directly evaluated. Angles ψ and η_f are shown in Figure 4, and must be calculated using the simple algebraic expressions below.

$$\hat{\mathbf{p}} = \hat{\mathbf{u}} \Rightarrow (\hat{\mathbf{u}}\cdot\hat{\mathbf{b}}_0) = -c\psi,\quad (\hat{\mathbf{u}}\cdot\hat{\mathbf{c}}_0) = s\psi \tag{A14}$$
$$\hat{\mathbf{p}} = \hat{\mathbf{t}} \Rightarrow (\hat{\mathbf{t}}\cdot\hat{\mathbf{b}}_0) = -s\psi,\quad (\hat{\mathbf{t}}\cdot\hat{\mathbf{c}}_0) = -c\psi$$

$$\begin{aligned}
(\hat{\mathbf{n}}\cdot\hat{\mathbf{r}}) &= s\eta_f\, s\psi\, s\delta + c\eta_f\, c\delta \\
(\hat{\mathbf{n}}\cdot\hat{\mathbf{b}}) &= c\eta_f\, s\psi\, s\delta - s\eta_f\, c\delta \\
(\hat{\mathbf{n}}\cdot\hat{\mathbf{c}}) &= c\psi\, s\delta
\end{aligned} \tag{A15}$$

$$\begin{aligned}
(\hat{\mathbf{s}}\cdot\hat{\mathbf{r}}) &= -c\lambda s\eta_f\, c\psi + s\lambda c\delta s\eta_f s\psi - s\lambda s\delta c\eta_f \\
(\hat{\mathbf{s}}\cdot\hat{\mathbf{b}}) &= -c\lambda c\eta_f\, c\psi + s\lambda c\delta c\eta_f s\psi + s\lambda s\delta s\eta_f \\
(\hat{\mathbf{s}}\cdot\hat{\mathbf{c}}) &= c\lambda\, s\psi + s\lambda c\delta c\psi
\end{aligned} \tag{A16}$$

where

$$s\eta_f = R/r; \quad c\eta_f = -z'/r; \quad s\psi = t'/R; \quad c\psi = u'/R \tag{A17}$$

and where $r = |\mathbf{x}_s - \mathbf{x}|$ is straight-line distance from $\mathbf{x}_s$ to $\mathbf{x}$, and R is cylindrical radius from $\mathbf{x}_s$ to $\mathbf{x}$.

All the above terms in the radiation pattern can be evaluated for two special source points on the fault, namely $\mathbf{x} = \mathbf{x}_h$, the hypocenter, and $\mathbf{x} = \mathbf{x}_c$, the closest point to the station.

For $\mathcal{R}_p(\mathbf{x}_s,\mathbf{x}_h)$ where, the hypocenter $\mathbf{x}_h = (u_h, v_h, 0)$ (A18)

- $r = r_h$, hypocentral distance
- $R = R_h = \sqrt{r_h^2 - d_h^2}$, epicentral distance
- d_h= depth of the hypocenter from the free surface
- $u' = u_s - u_h$
- $z' = z_h = -d_h$, z-coordinate (elevation) of the hypocenter
- $t' = \dfrac{-w_s}{s\delta} - \left(\dfrac{d_o}{s\delta} + v_h\right)c\delta.$

d_o = depth to top of slipped zone

and

.For $\mathcal{R}_p(\mathbf{x}_s,\mathbf{x}_c)$ where $\mathbf{x}_c = (u_c, v_c, w_c)$, the closest point, (A19)

- $r = r_r$ rupture distance
- $z' = z_c = -\left(\dfrac{d_o}{s\delta} + v_c\right)s\delta$, z-coordinate (elevation) of the closest point
- $R = R_c = \sqrt{r_r^2 - z'^2}$, horizontal distance from station to closest point
- $u' = u_s - u_c$
- $t' = \dfrac{-w_s}{s\delta} - \left(\dfrac{d_o}{s\delta} + v_c\right)c\delta$, and
- d_o = distance to the top of the slipped zone.

A Possible Simplification

If forced to simplify the radiation patterns, we would set $\eta_f = 90\circ$, which corresponds to rays travelling horizontally leaving the source. Owing to the increase of S velocity with depth, this approximation will usually not be too bad, but we have not made many calculations to verify the general accuracy of this approximation.

APPENDIX B, ISOCHRONE VELOCITY MODIFICATION FACTORS

We introduce a modification factor m_5 to account for the situation when the station is off the end of the fault (e.g. station1 in Figure 2), and *D* is very small.

We use the arrival time difference

$$\delta t_a = t_a(\mathbf{x}_c) - t_a(\mathbf{x}_h) \quad = \frac{D}{\tilde{c}'\beta} \tag{B1}$$

to test whether the hypocenter and the closest point are near each other at the edge of the fault. We compare this arrival time difference to Δt_a^q, the arrival time difference if the hypocenter were at the center of the fault.

Algorithm

<u>IF</u> $\mathbf{x}_c$ is NOT on the edge of the fault, then $m_5 = 1$

<u>ELSE</u> $Q = \sqrt{\left(u_c - \frac{L}{2}\right)^2 + \left(v_c - \frac{W}{2}\right)^2}$ is the distance on the fault from its center to $\mathbf{x}_c$, κ = 2 (an adjustable parameter, meant to be approximately Q/a_q, where a_q is comparable to the width of the slip tapering zone in km (equation 11).

$$\Delta t_a^q = \frac{Q}{\kappa\beta}\left(\frac{\beta}{v_r} - 1\right), \text{ and } m_5 := \min\left(1, \frac{\delta t_a}{\Delta t_a^q}\right). \tag{B2}$$

Based on equation 11, κ should be 3, but we suspect κ = 2 is a better number given the finite width of isochrones.

ACKNOWLEDGMENTS

The authors thank David M. Boore, Jon B. Fletcher, and Robert Youngs, who reviewed this report.

This project was sponsored by the Pacific Earthquake Engineering Research Center's Program of Applied Earthquake Engineering Research of Lifeline Systems supported by the California Energy Commission, California Department of Transportation, and the Pacific Gas & Electric Company. The financial support of the PEARL sponsor organizations including the Pacific Gas & Electric company, the California Energy Commission, and the California Department of Transportation is acknowledged. This work made use of Earthquake Engineering Research Centers Shared Facilities supported by the National Science Foundation under Award Number EEC-9701568.

Legal Notice

This report was prepared as a result of work sponsored by the California Energy Commission (Commission). It does not necessarily represent the view of the Commission, its employees, or the State of California. The Commission, the State of California, its employees, Contractors and subcontractors make no warranty, express or implied, and assume no legal liability for the information in this report; nor does any party represent that the use of this information will not infringe upon privately owned rights. This report has not been approved or disapproved by the Commission nor has the commission passed upon the accuracy or adequacy of the information in this report.

REFERENCES

Abrahamson, N., 2003. Draft plan for 1-D rock motion simulations, unpublished report, Next Generation Attenuation of Ground Motions (NGA) Project, PEER Lifelines Research Program, Pacific Earthquake Engineering Research Center, University of California, Berkeley.

Abrahamson, N., and Shedlock, K., 1997. Overview, Seismological Research Letters, v. 68, pp. 9-23.

Aki, K., and Richards, P., 1980, *Quantitative Seismology*, Freeman, San Francisco.

Boore, D., 1983. Stochastic simulation of high frequency ground motions based on seismological models of radiated spectra, Bulletin of the Seismological Society of America, v. 73, 1865-1894.

Boore D. and W. B. Joyner, 1997. Site amplification for generic rock sites, Bulletin of the Seismological Society of America, v. 87, 327-341.

Graves, R. W. and A. Pitarka, 2004. Broadband time history simulation using a hybrid approach, Proc. 13th World Conf. Earthq. Eng., Vancouver, Canada, paper no. 1098.

Boore, D.M. and Boatwright, J., 1984, Average body wave radiation coefficients, Bull. Seismol. Soc. Am., v. 74, 1615-1622.

Heaton, T.H., 1990, Evidence for and implications of self-healing pulses of slip in earthquake rupture: Phys. Earth Planet. Inter., v. 64, 1-20.

Joyner, W.B., and Spudich, P., 1994, Including near-field terms in the isochrone integration method for application to finite-fault or Kirchhoff boundary integral problems: Bulletin of the Seismological Society of America, v. 84, 1260-1265.

Mai, P.M., and Beroza, G.C., 2002, A spatial random field model to characterize complexity in earthquake slip, J. Geophys Res., v. 107(B11), 2308, doi:10.1029/2001JB000588.

Pitarka, A., Somerville, P., Fukushima, Y., Uetake, T., and Irikura, K., 2000, Simulation of Near-Fault Strong Ground Motion Using Hybrid Green's Function: Bulletin of the Seismological Society of America, v. 90, 566-586.

Rogers, A.M., and Perkins, D.M., 1996. Monte Carlo simulation of peak-acceleration attenuation using a finite-fault uniform-patch model including isochron and extremal characteristics, Bulletin of the Seismological Society of America, v. 86, pp. 79-92.

Somerville, P.G., Smith, N.F., Graves, R.W., and Abrahamson, N.A., 1997, Modification of empirical strong ground motion attenuation relations to include the amplitude and duration effects of rupture directivity: Seismol. Res. Lett., v. 68, 199-222.

Spudich, P., and Frazer, L.N., 1984, Use of ray theory to calculate high frequency radiation from earthquake sources having spatially variable rupture velocity and stress drop: Bulletin of the Seismological Society of America, v. 74, 2061-2082.

Spudich, P., and Frazer, L.N., 1987, Errata: Bulletin of the Seismological Society of America, v. 77, 2245.

Spudich, P, and Xu, L.., 2003. Documentation of software package ISOSYN: Isochrone integration programs for earthquake ground motion calculations, CD accompanying IASPEI *International Handbook of Earthquake and Engineering Seismology*, 72 pp.

FIGURE CAPTIONS

Figure 1. Isochrone theory example for a vertical strike-slip fault 170 km long and 17 km wide, with a station located 1 km off the fault at -30 km along strike. Star is hypocenter location. Red triangle is the point on the fault closest to the station. a) Contours are circular rupture front positions at 5 s intervals. Color fill is slip amplitude, which is 1.0 m over most of the fault and tapers to zero at the edges. b) Contours are S wave travel time from each point on the fault to the station. Color fill is slip amplitude. c) Contours are arrival time function (sum of rupture time plus S wave travel time). Contours are isochrones, paths of integration in (A3). Colors are isochrone velocity. At every point on the fault the isochrone velocity is proportional to the spacing between the local isochrones. d) Contours are arrival time function (isochrones, paths of integration). Colors are the real part of the integrand of equation (A3) for transverse (FN) motion. Ground displacement at time *t* is proportional to the integral of the integrand along the isochrone for time *t*. Boundary between blue and red is the node of the radiation pattern for transverse motion. Integrand is large near $\mathbf{x}_c$ because station is very close to fault there.

Figure 2. Schematic illustration of approximate isochrone velocity $\tilde{c}$ for two stations, triangles labeled 1 and 2. $\mathbf{x}_{c_1}$ and $\mathbf{x}_{c_2}$ are closest points on fault to stations 1 and 2, respectively. Note that $\mathbf{x}_{c_1}$ is on the edge of the fault but $\mathbf{x}_{c_2}$ is within the fault. Star is hypocenter. D is distance on the fault from the hypocenter to the closest point.

Figure 3. Relation of fault coordinate system to geographic coordinate system. Let u be distance along strike and v be distance down dip from the origin of coordinates O on the rectangular slipped area (pink) of the fault, and let d_o be the depth to the origin of the (u,v,w) coordinate system, i.e. d_o is depth to the top of the slipped zone. Let $\hat{\mathbf{z}}$ point upward. Then a point $\mathbf{x}$ on the fault has coordinates $\mathbf{x} = (u,v,0)$. The fault perpendicular (transverse) unit vector in the horizontal plane is $\hat{\mathbf{t}} = -(\hat{\mathbf{u}} \times -\hat{\mathbf{z}})$. Fault-parallel motion is directed along the $\hat{\mathbf{u}}$ direction and fault-normal motion is directed along the $\hat{\mathbf{t}}$ direction.

Figure 4. Geometry for calculating radiation patterns and ray geometry.

Figure 5. Illustration of 3-segment rupture. $\mathbf{x}_h$ is the event hypocenter. $\mathbf{x}_h^2$ and $\mathbf{x}_h^3$ are pseudo-hypocenters placed on segments 2 and 3 at the same depth as $\mathbf{x}_h$. Horizontal line segments s_1, s_2, s_3 and downdip segment d_3 are analogous to segments s and d in Figure 2. $\mathbf{x}_c^1$, $\mathbf{x}_c^2$, and $\mathbf{x}_c^3$ are the points on each segment closest to the station (pink triangle) at . $\mathbf{x}_s$. r_r is the distance to the closest point on any fault segment.

Figure 6. Maps of approximate isochrone velocity ratio (left side) and fault-normal average radiation patterns (right side) around a multisegment approximation (black line) of the rupture of the 1992 Landers, California, earthquake. Epicenter is at (0,0). Spatial discontinuities in plotted quantities are caused by the closest point jumping from segment to segment.

Figure 7. Map of residuals for M6.5 strike slip event SA with hypocenter 02 (turquoise dot). Residuals are defined as ln(synthetic data) minus ln(best fitting non-directive model). 25 km long fault lies along the X=0 axis, symmetrically disposed about Y=0. Positive Y is nominal "north." Three maps show residuals for geometric average, fault-normal ($\hat{\mathbf{t}}$) and fault-parallel ($\hat{\mathbf{u}}$) components of motion. Red shows synthetic data greater than fitted non-directive model; blue shows the opposite.

Figure 8. Same as 7, with green bars in various locations on the geometric-average map indicating probable polarization of S waves. At some locations the S wave polarization is parallel to the fault-oriented coordinate system (X,Y) and at other locations the S wave polarization is rotated 45° from the fault coordinate system.

Figure 9. Same as 7, but with area of FN polarization circled. The small FP motions drag down the geometric average in the circled region. This is problematic because in real data the amplitude of the FP motion in the circled region is controlled by unmodelable factors.

Figure 10. Map of residuals for M6.5 strike slip event SA with hypocenter 04 (turquoise dot). Because SA is a short fault, the residual map is nearly identical to that for SA02 (Figure 7). See Figure 7 caption for details.

Figure 11. Summary plot of residuals for M6.5 strike-slip event SA compared to two predictor variables, $\ln(A_1^p) = \ln(m_5\, \tilde{c}'\, \overline{\mathcal{R}}_{ga})$ and $\ln(A_3^p) = \ln(D\, \tilde{c}'\, \overline{\mathcal{R}}_{ga})$. Upper scatter plots show geometric average residuals from all 24 realizations compared with geometric average predictor variables. Blue lines are best-fitting straight lines, and red lines are local regression curves. Lower two rows show maps of geometric average residuals and predictors for realizations (hypocenters) 02 (upper row) and 04 (lower row). Maps are rotated so that nominal north (+Y) is to the right. Residual maps (far right column) are from Figures 7 and 10. Other two columns show maps of the two predictor variables for each hypocenter location (turquoise dot).

Figure 12. Demonstration that FN (middle column) and FP (right column) residuals for M6.5 strike-slip event SA are better predicted individually by predictor variables than is the geometric average (left column). Residuals are from all 24 realizations of M6.5 strike-slip event SA. Blue lines are best-fitting straight lines, and red lines are smooth curves passed though the data in an optimal way. Upper row is predictor $\ln(A_1^p)$; lower row is predictor $\ln(A_3^p)$.

Figure 13. Summary plot of residuals for M6.5 reverse event RB compared to two predictor variables, $\ln(A_1^p) = \ln(m_5\, \tilde{c}'\, \overline{\mathcal{R}}_{ga})$ and $\ln(A_3^p) = \ln(D\, \tilde{c}'\, \overline{\mathcal{R}}_{ga})$. Upper scatter plots show geometric average residuals from all 24 realizations compared with geometric average predictor variables. Blue lines are best-fitting straight lines, and red lines are local regression curves. Lower two rows show maps of geometric average residuals and predictors for realizations (hypocenters) 02 (upper row) and 04 (lower row). Maps are rotated so that nominal north (+Y) is to the right. Hypocenter shown by turquoise dot; vertical projection of fault surface shown by barely visible black rectangle. Residual maps (far right column) are from Figures 7 and 10. Other two columns show maps of the two predictor variables for each hypocenter location.

Figure 14. Demonstration that FN (middle column) and FP (right column) residuals for M6.5 reverse event RB are better predicted individually by predictor variables than is the geometric average (left column). Residuals are from all 24 realizations of the event. Blue lines are best-fitting straight lines, and red lines are smooth curves passed though the data in an optimal way. Upper row is predictor $\ln(A_1^p)$; lower row is predictor $\ln(A_3^p)$.

Figure 15. Summary plot of residuals for M7.0 reverse event RG compared to two predictor variables, $\ln(A_1^p) = \ln(m_5\, \tilde{c}'\, \overline{\mathcal{R}}_{ga})$ and $\ln(A_3^p) = \ln(D\, \tilde{c}'\, \overline{\mathcal{R}}_{ga})$. Upper scatter plots show geometric average residuals from all 24 realizations

compared with geometric average predictor variables. Blue lines are best-fitting straight lines, and red lines are local regression curves. Lower two rows show maps of geometric average residuals for realizations (hypocenters) 02 (upper row) and 04 (lower row). Maps of predictors not available at time of writing. Maps are rotated so that nominal north (+Y) is to the right. Hypocenter shown by turquoise dot; vertical projection of fault surface shown by barely visible balck rectangle. Residual maps (far right column) are from Figures 7 and 10.

Figure 16. Demonstration that FN (middle column) and FP (right column) residuals for M7.0 reverse event RG are better predicted individually by predictor variables than is the geometric average (left column). Residuals are from all 24 realizations of the event. Blue lines are best-fitting straight lines, and red lines are smooth curves passed though the data in an optimal way. Upper row is predictor $\ln(A_1^p)$; lower row is predictor $\ln(A_3^p)$.

Figure 17. Summary plot of residuals for M7.5 reverse event RK compared to two predictor variables, $\ln(A_1^p) = \ln(m_5\, \tilde{c}'\, \overline{\mathcal{R}}_{ga})$ and $\ln(A_3^p) = \ln(D\, \tilde{c}'\, \overline{\mathcal{R}}_{ga})$. Upper scatter plots show geometric average residuals from all 24 realizations compared with geometric average predictor variables. Blue lines are best-fitting straight lines, and red lines are local regression curves. Lower two rows show maps of geometric average residuals and predictors for realizations (hypocenters) 02 (upper row) and 04 (lower row). Maps are rotated so that nominal north (+Y) is to the right. Hypocenter shown by turquoise dot; vertical projection of fault surface shown by barely visible balck rectangle. Residual maps (far right column) are from Figures 7 and 10. Other two columns show maps of the two predictor variables for each hypocenter location.

Figure 18. Demonstration that FN (middle column) and FP (right column) residuals for M7.5 reverse event RK are better predicted individually by predictor variables than is the geometric average (left column). Residuals are from all 24 realizations of the event. Blue lines are best-fitting straight lines, and red lines are local regression curves. Upper row is predictor $\ln(A_1^p)$; lower row is predictor $\ln(A_3^p)$.

a) Contours of rupture time over color plot of slip amplitude

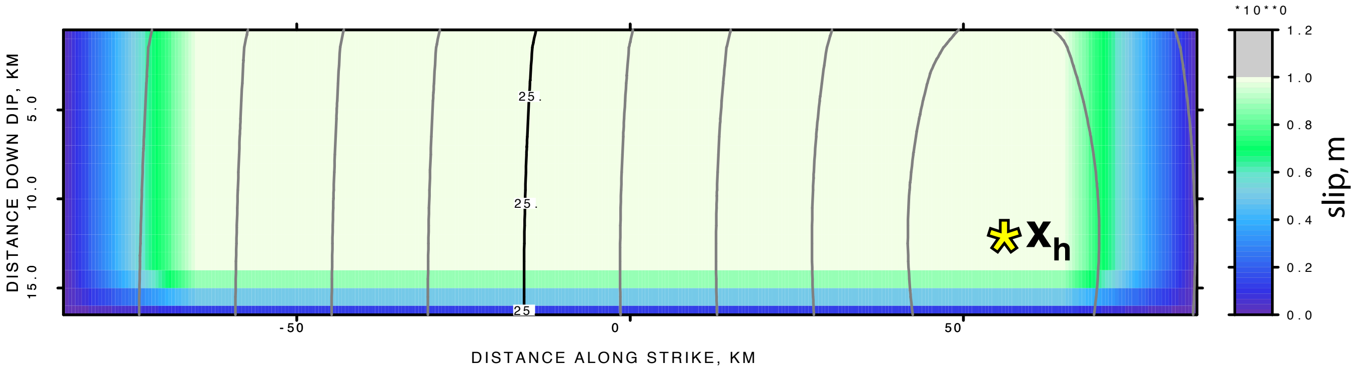

b) Contours of S wave travel time over color plot of slip amplitude

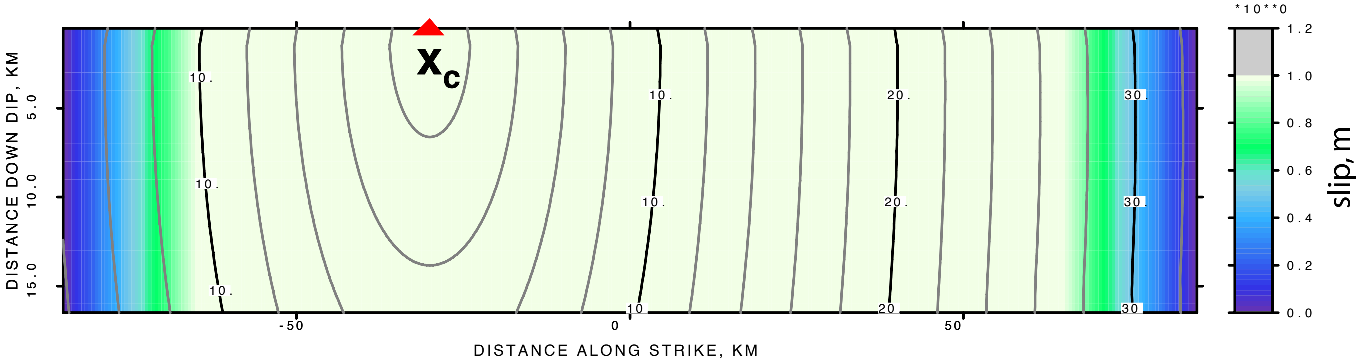

c) Contours of arrival time (= rupture time + S travel time) over color plot of isochrone velocity

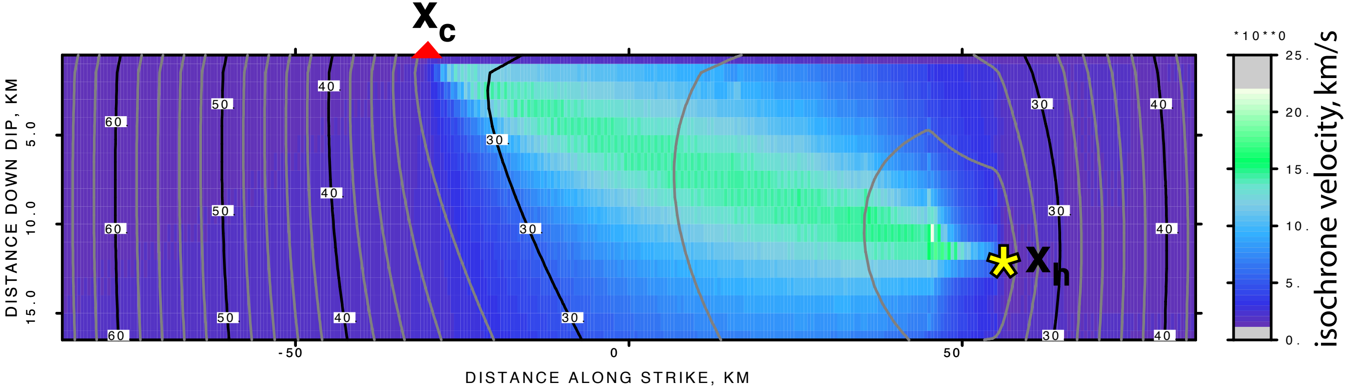

d) Contours of arrival time over color plot of integrand for fault-normal motion

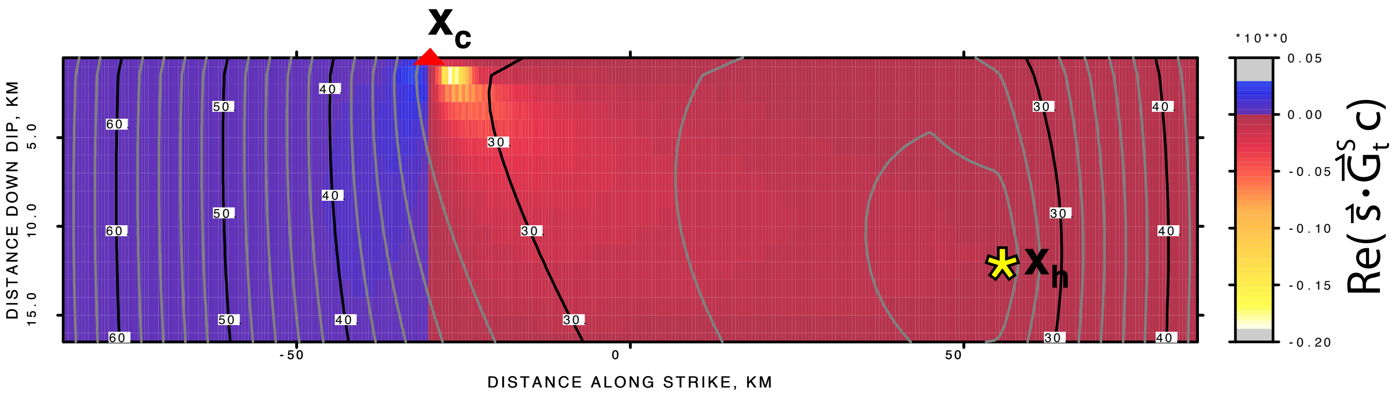

Figure 1

$$\tilde{c} \sim D / \left(t_a(\mathrm{hypo}) - t_a(\mathrm{closest}) \right)$$

$$\tilde{c}' = \tilde{c} / V_S$$

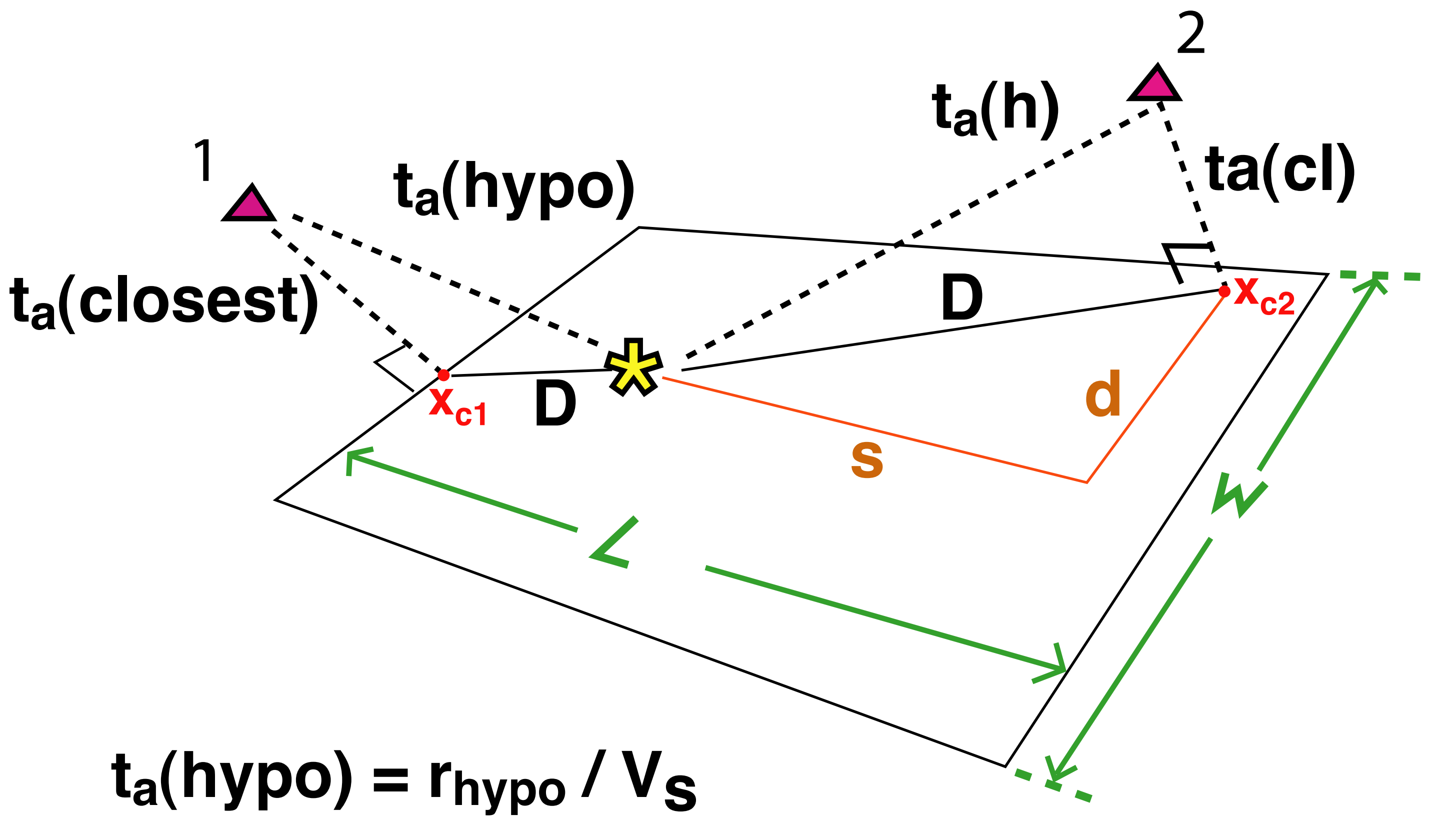

$$t_a(\mathrm{hypo}) = r_{\mathrm{hypo}} / V_S$$

$$t_a(\mathrm{closest}) = D/V_r + r_r/V_S$$

$$D = \mathrm{sqrt}(\, d^2 + s^2)$$

Figure 2

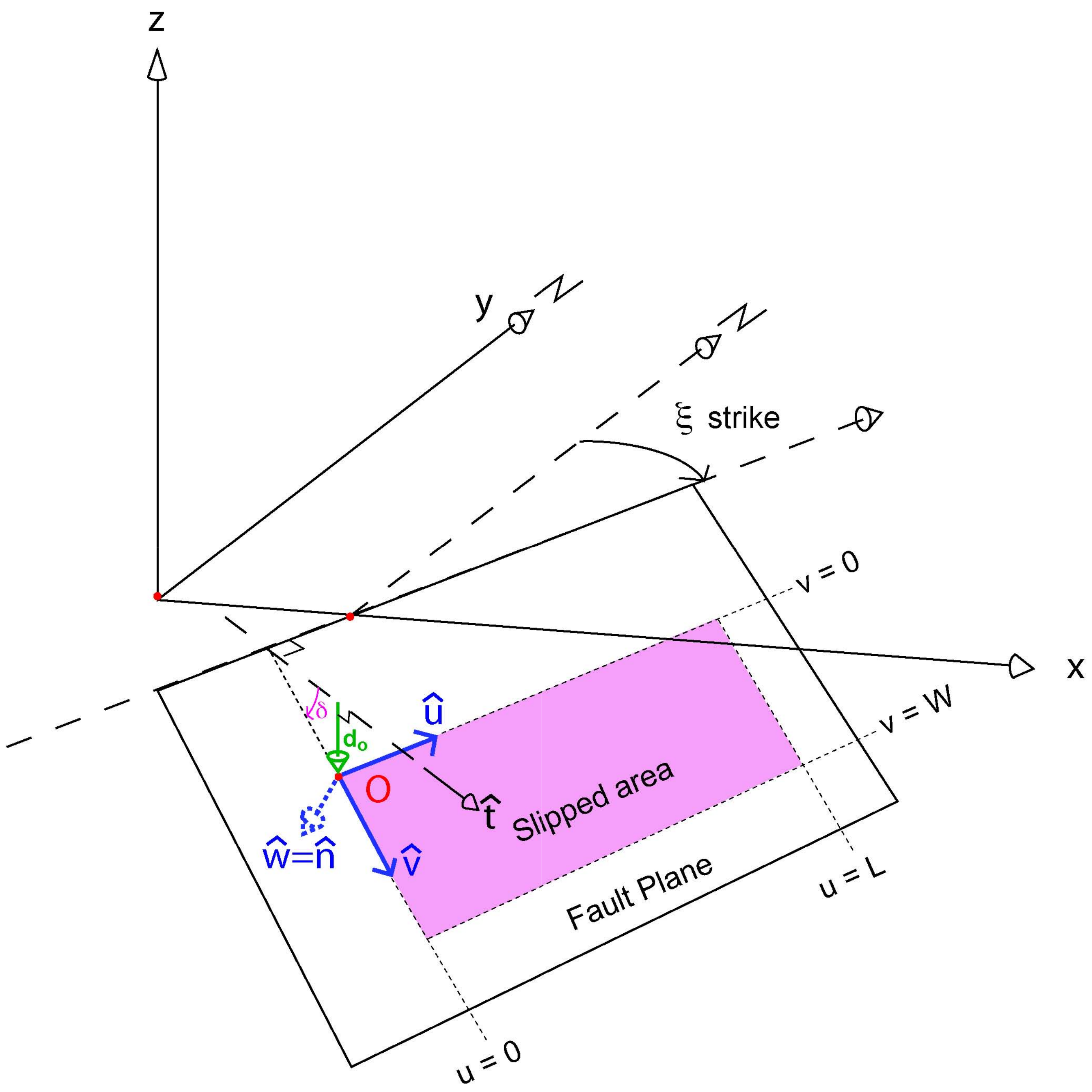
z
y
N
N
ξ strike
x
v = 0
v = W
δ
d_o
$\hat{u}$
O
$\hat{t}$
Slipped area
$\hat{w}=\hat{n}$
$\hat{v}$
Fault Plane
u = L
u = 0

Figure 3

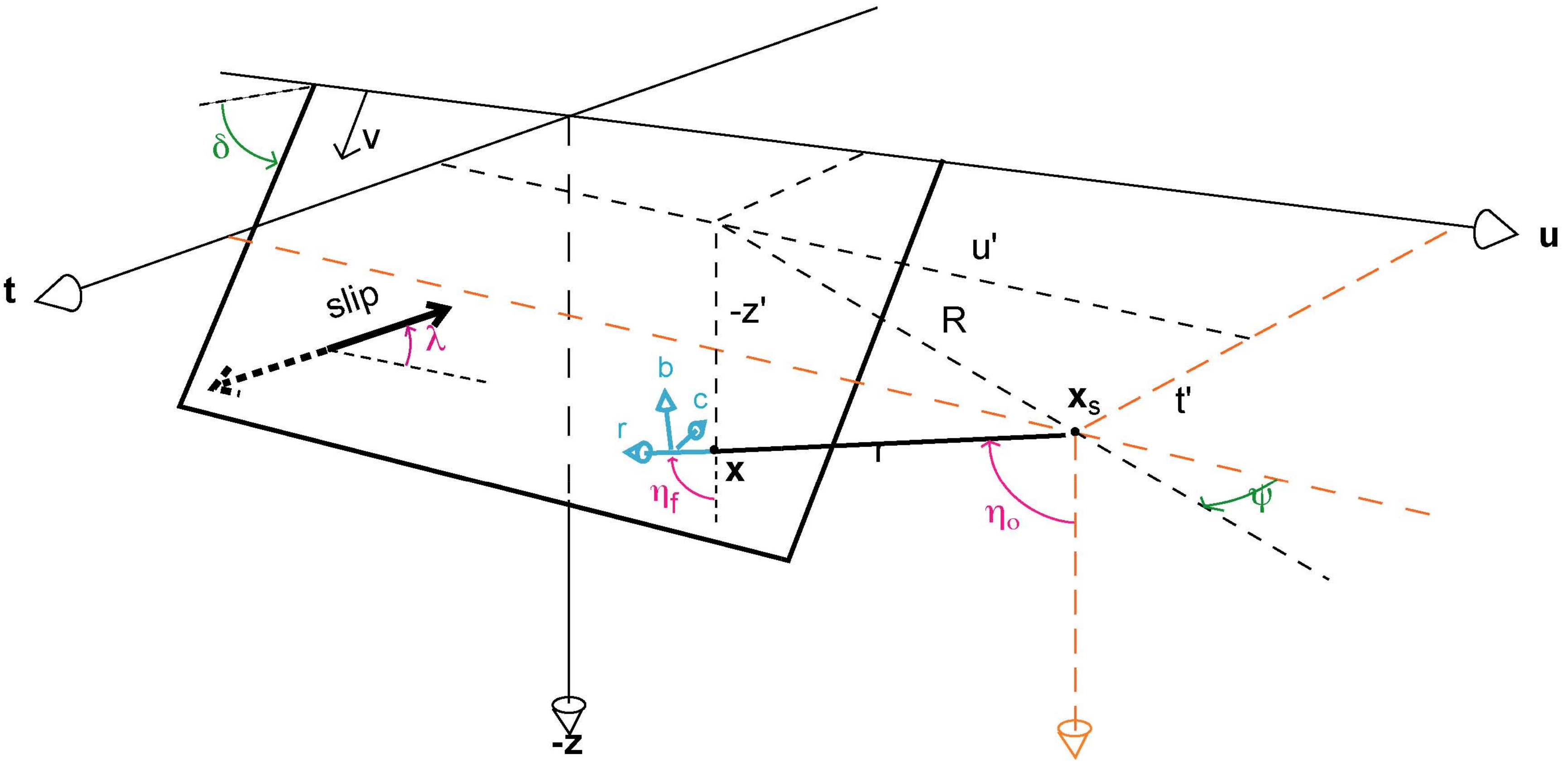

figure 4

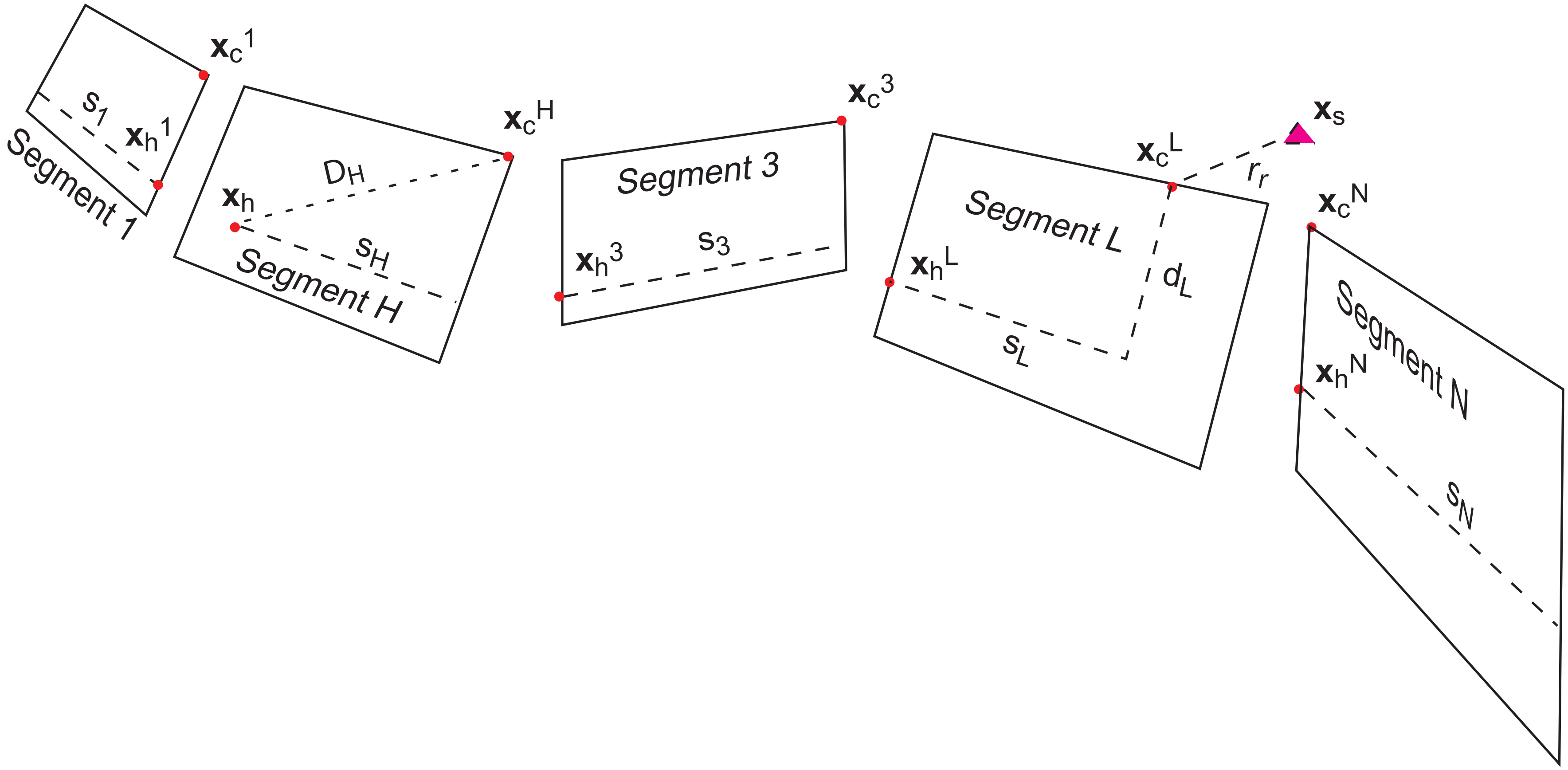

$\mathbf{x}_c{}^1$
s_1
$\mathbf{x}_h{}^1$
Segment 1
$\mathbf{x}_c{}^H$
D_H
$\mathbf{x}_h$
s_H
Segment H
$\mathbf{x}_c{}^3$
Segment 3
$\mathbf{x}_h{}^3$
s_3
$\mathbf{x}_c{}^L$
$\mathbf{x}_s$
r_r
Segment L
$\mathbf{x}_h{}^L$
d_L
s_L
$\mathbf{x}_c{}^N$
Segment N
$\mathbf{x}_h{}^N$
s_N

Figure 5

Maps of approximate isochrone velocity ratio and average FN radiation pattern for model of 1992 Landers earthquake

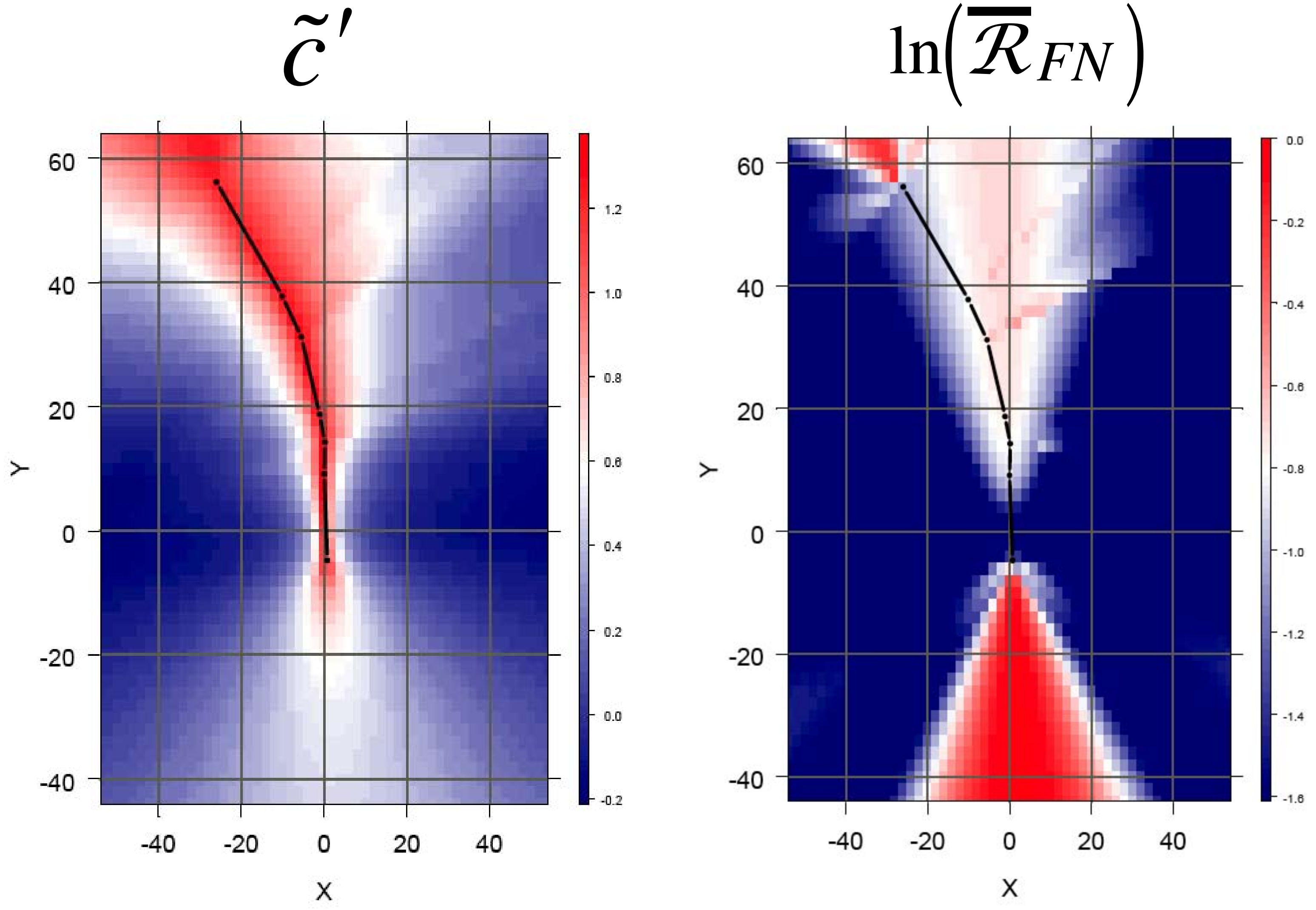

$\tilde{c}'$

$\ln\left(\overline{\mathcal{R}}_{FN}\right)$

Figure 6

SA02, map of GA, FN, FP resids

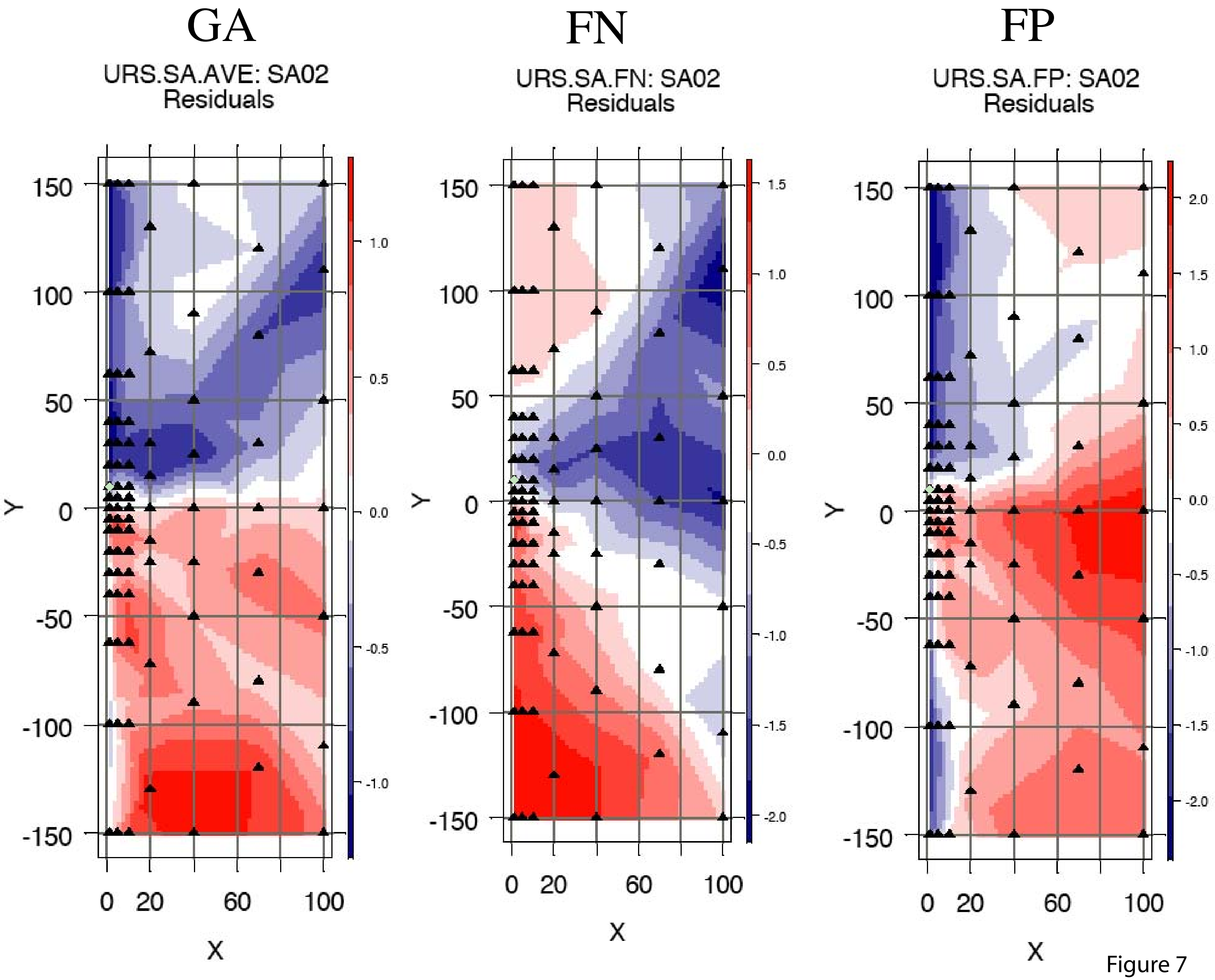

GA

URS.SA.AVE: SA02 Residuals

FN

URS.SA.FN: SA02 Residuals

FP

URS.SA.FP: SA02 Residuals

Figure 7

SA02, S wave polarizations

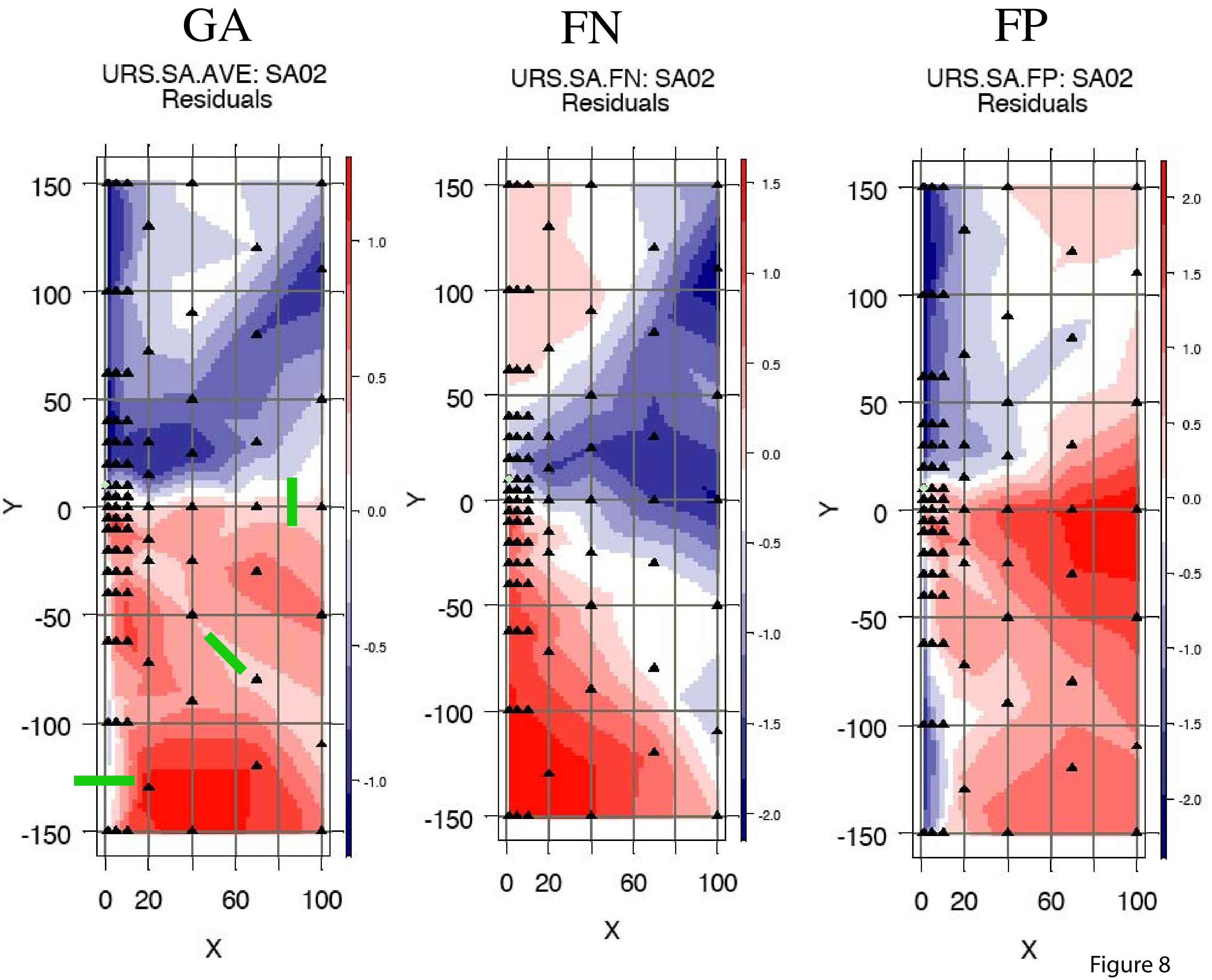

Figure 8

An example of misleading geometric average

GA FN FP

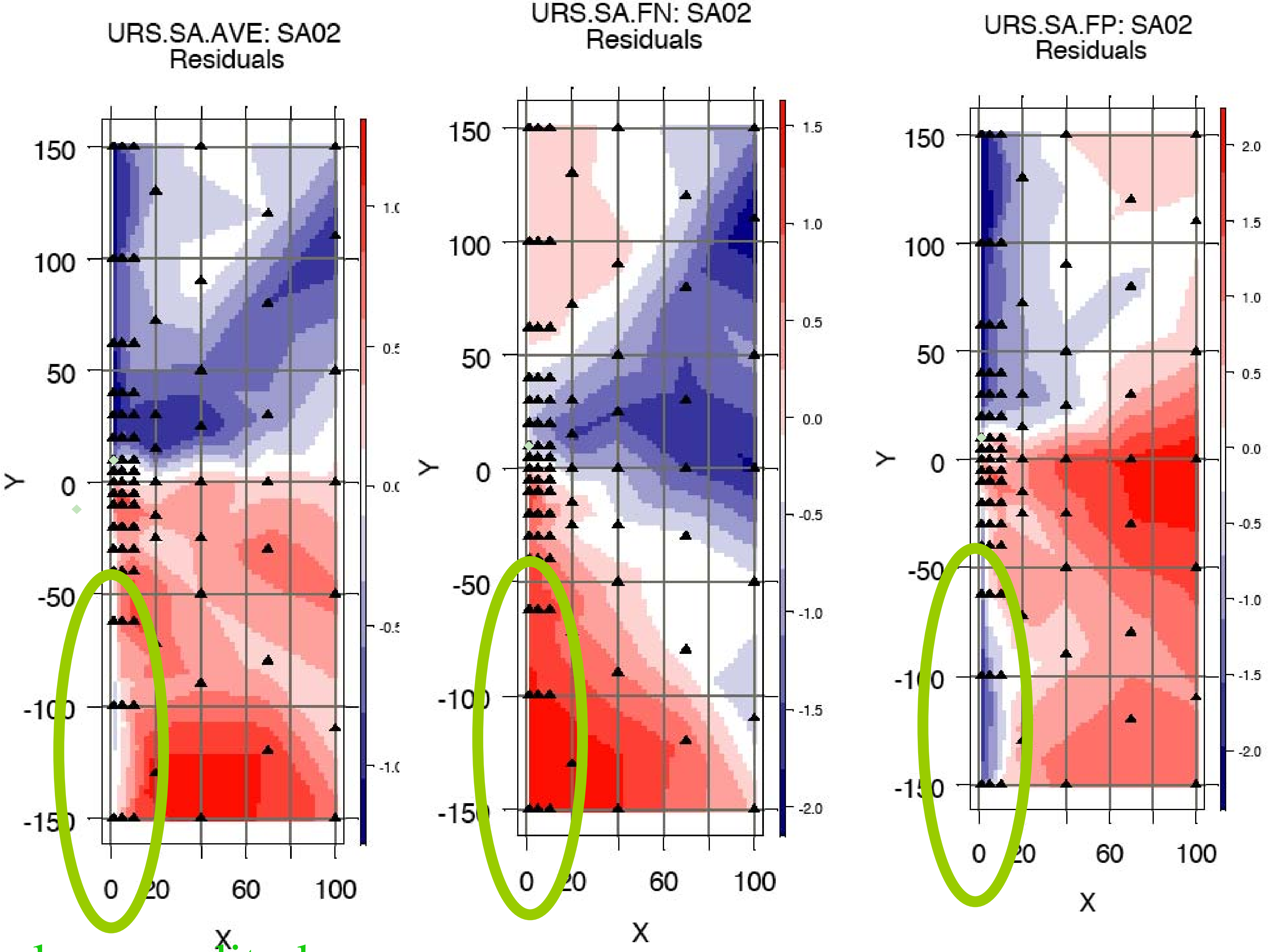

low amplitude

biggest amplitudes

Figure 9

SA04, map of GA, FN, FP resids

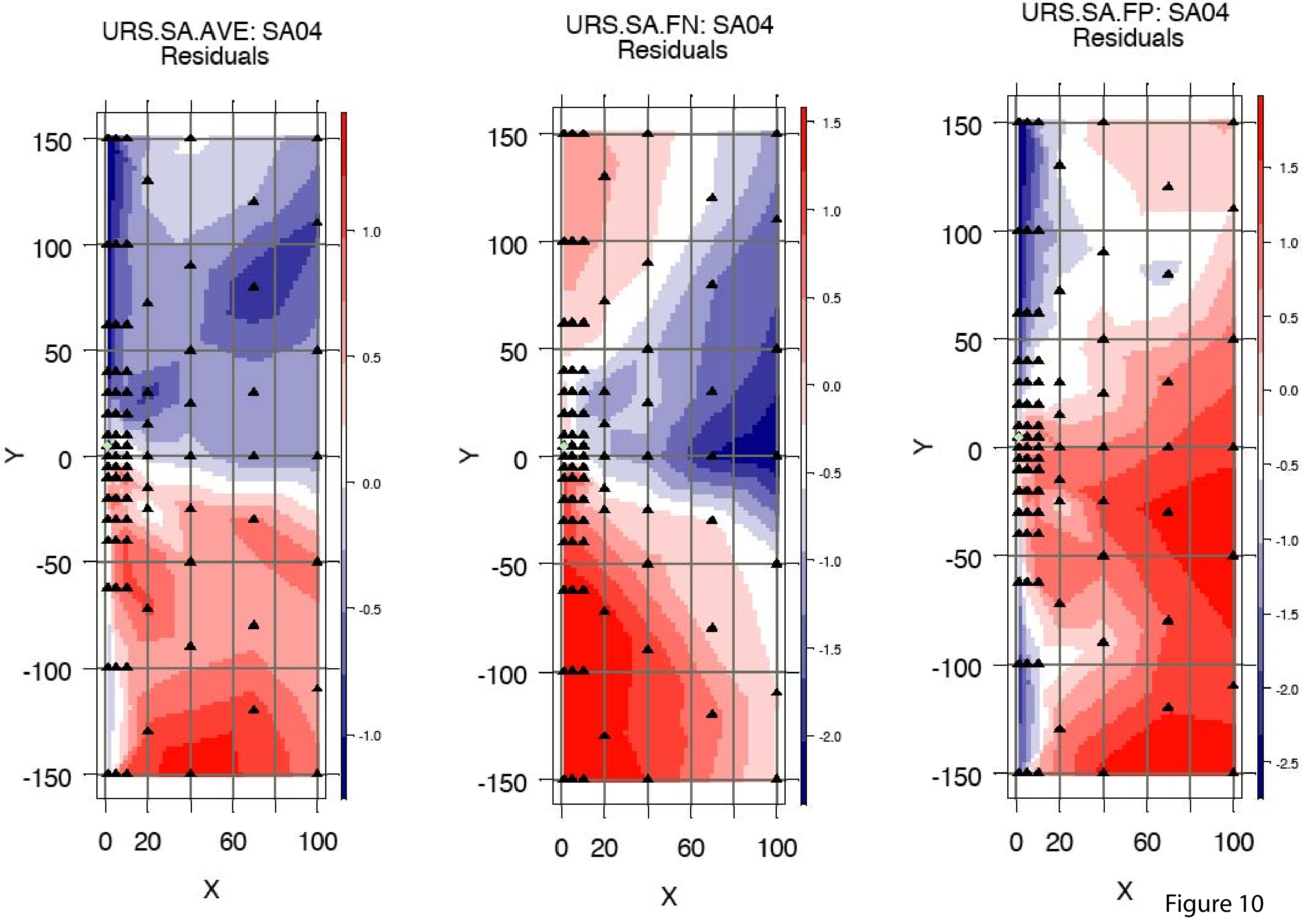

GA

FN

FP

Figure 10

SA, geom
avg comp

residual

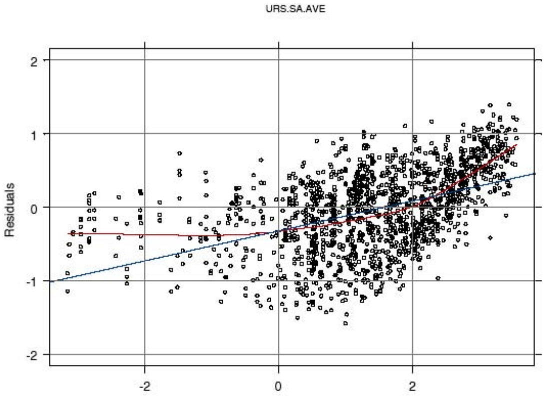

$\ln(D\,\tilde{c}'\,\overline{\mathcal{R}}_{ga})$

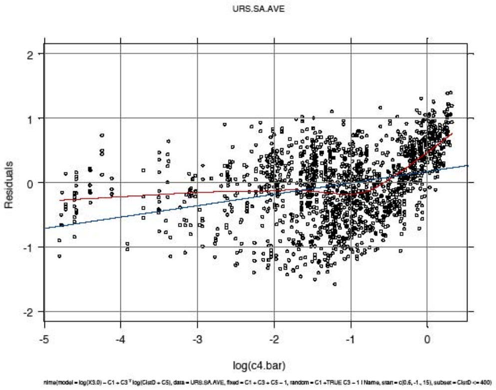

$\ln(m_5\,\tilde{c}'\,\overline{\mathcal{R}}_{ga})$

map of $\ln(D\,\tilde{c}'\,\overline{\mathcal{R}}_{ga})$

map of $\ln(m_5\,\tilde{c}'\,\overline{\mathcal{R}}_{ga})$

map of residuals

hypo
02

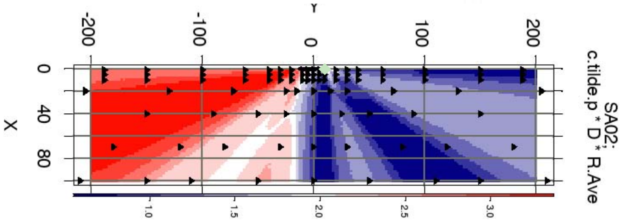

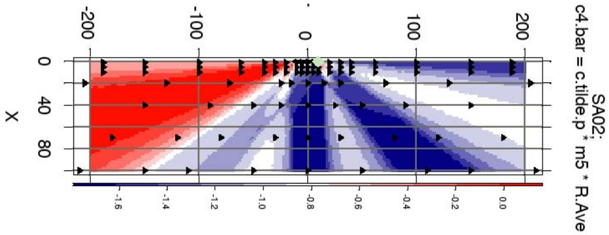

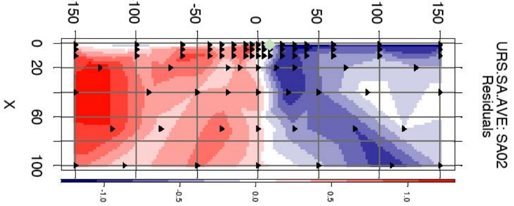

hypo
04

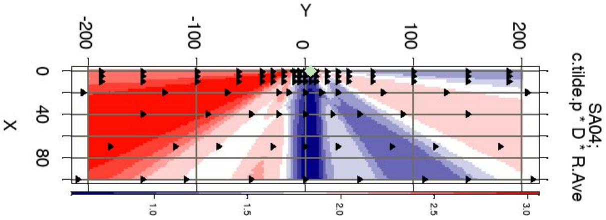

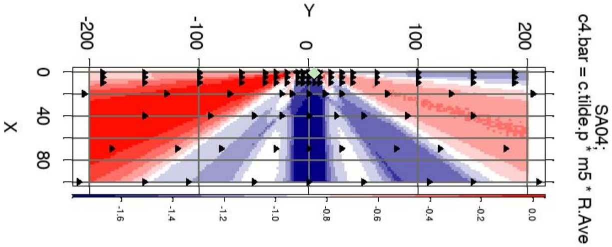

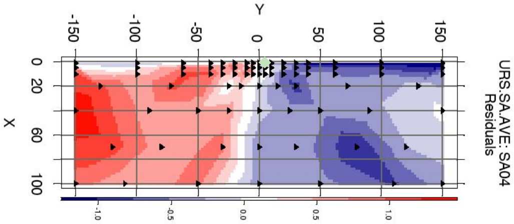

Figure 11

SA residuals vs two predictors

Geom Avg FN FP

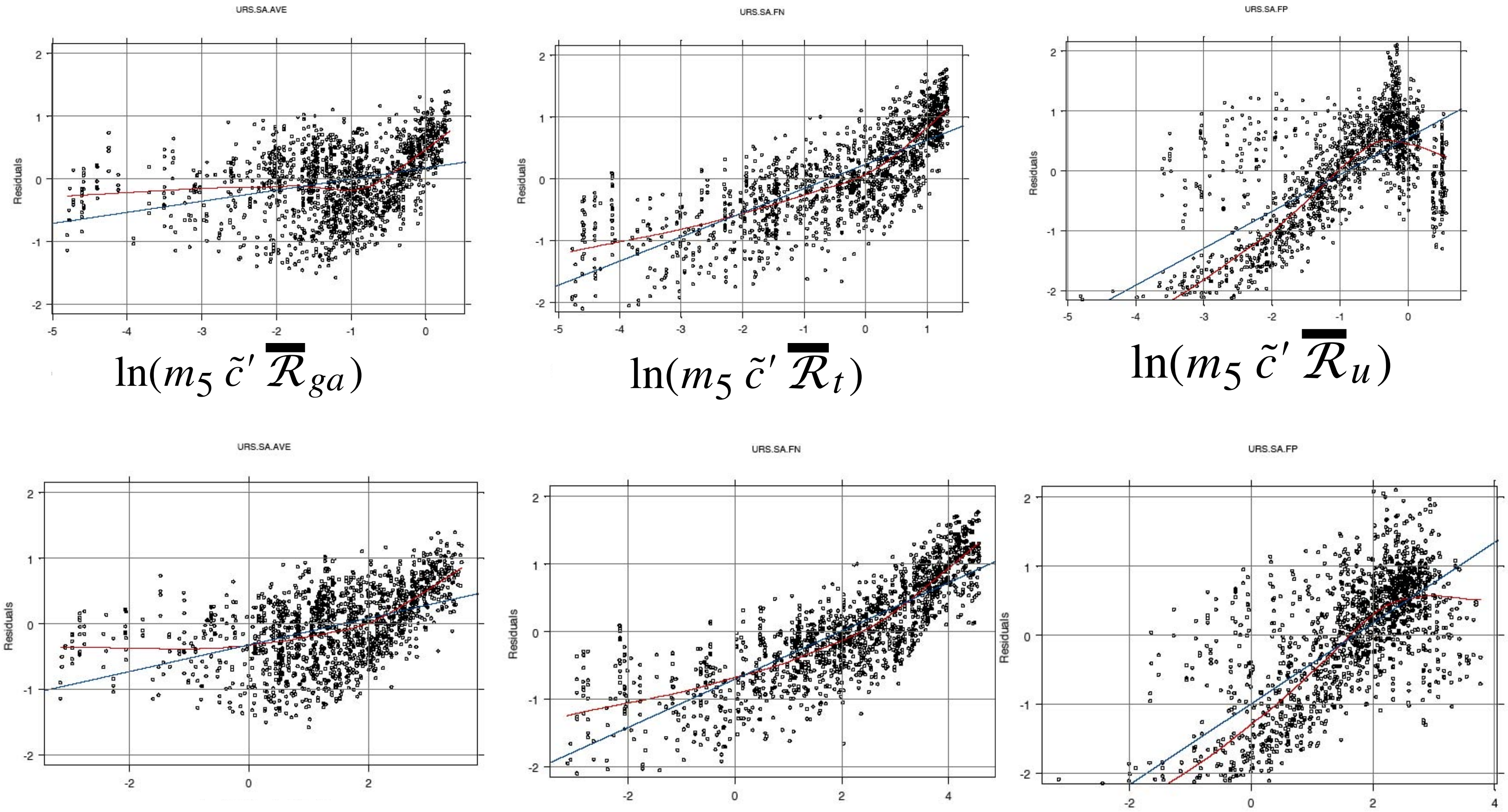

residual

$\ln(m_5\, \tilde{c}'\, \overline{\mathcal{R}}_{ga})$ $\ln(m_5\, \tilde{c}'\, \overline{\mathcal{R}}_{t})$ $\ln(m_5\, \tilde{c}'\, \overline{\mathcal{R}}_{u})$

residual

$\ln(D\, \tilde{c}'\, \overline{\mathcal{R}}_{ga})$ $\ln(D\, \tilde{c}'\, \overline{\mathcal{R}}_{t})$ $\ln(D\, \tilde{c}'\, \overline{\mathcal{R}}_{u})$

Figure 12

residual

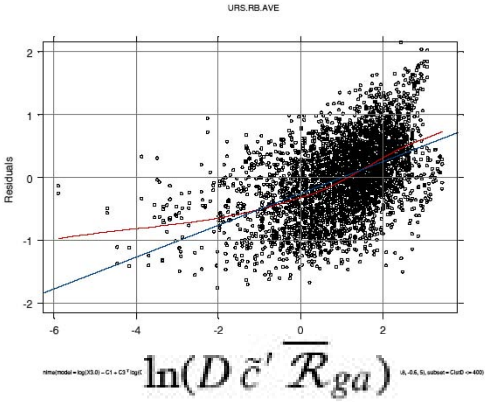

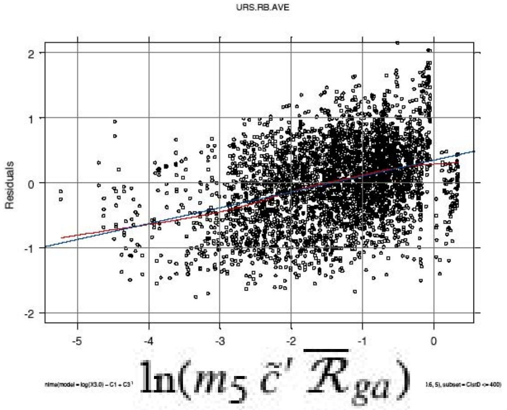

RB, geom avg comp

map of $\ln(D\,\tilde{c}'\,\overline{\mathcal{R}}_{ga})$

map of $\ln(m_5\,\tilde{c}'\,\overline{\mathcal{R}}_{ga})$

map of residuals

hypo 02

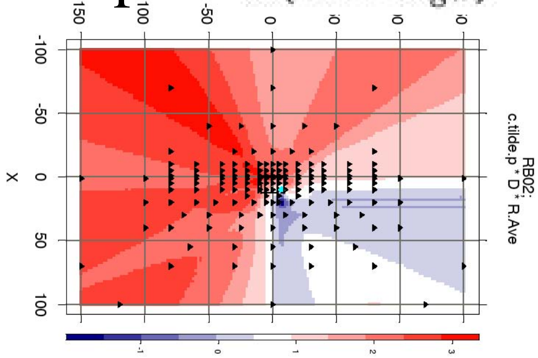

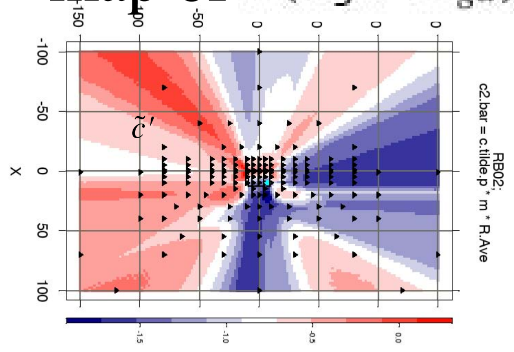

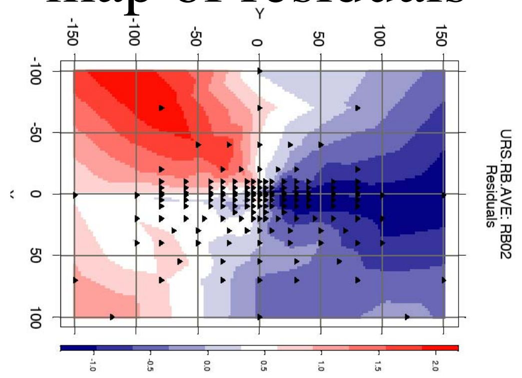

hypo 04

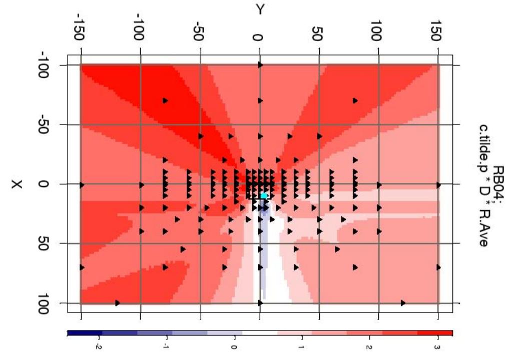

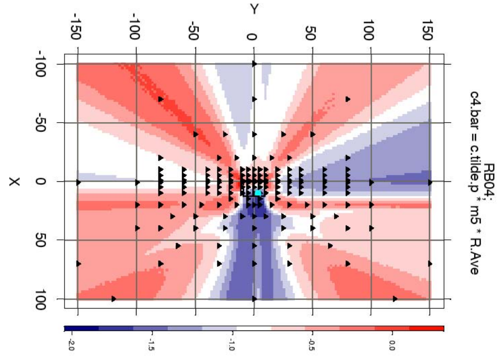

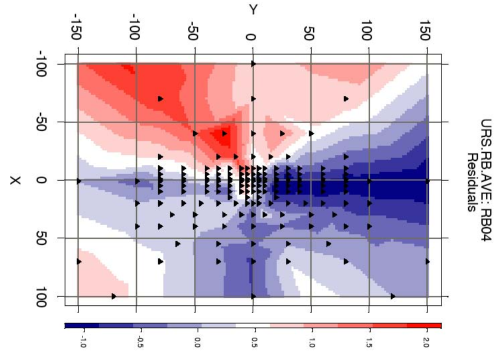

Figure 13

RB residuals vs two predictors

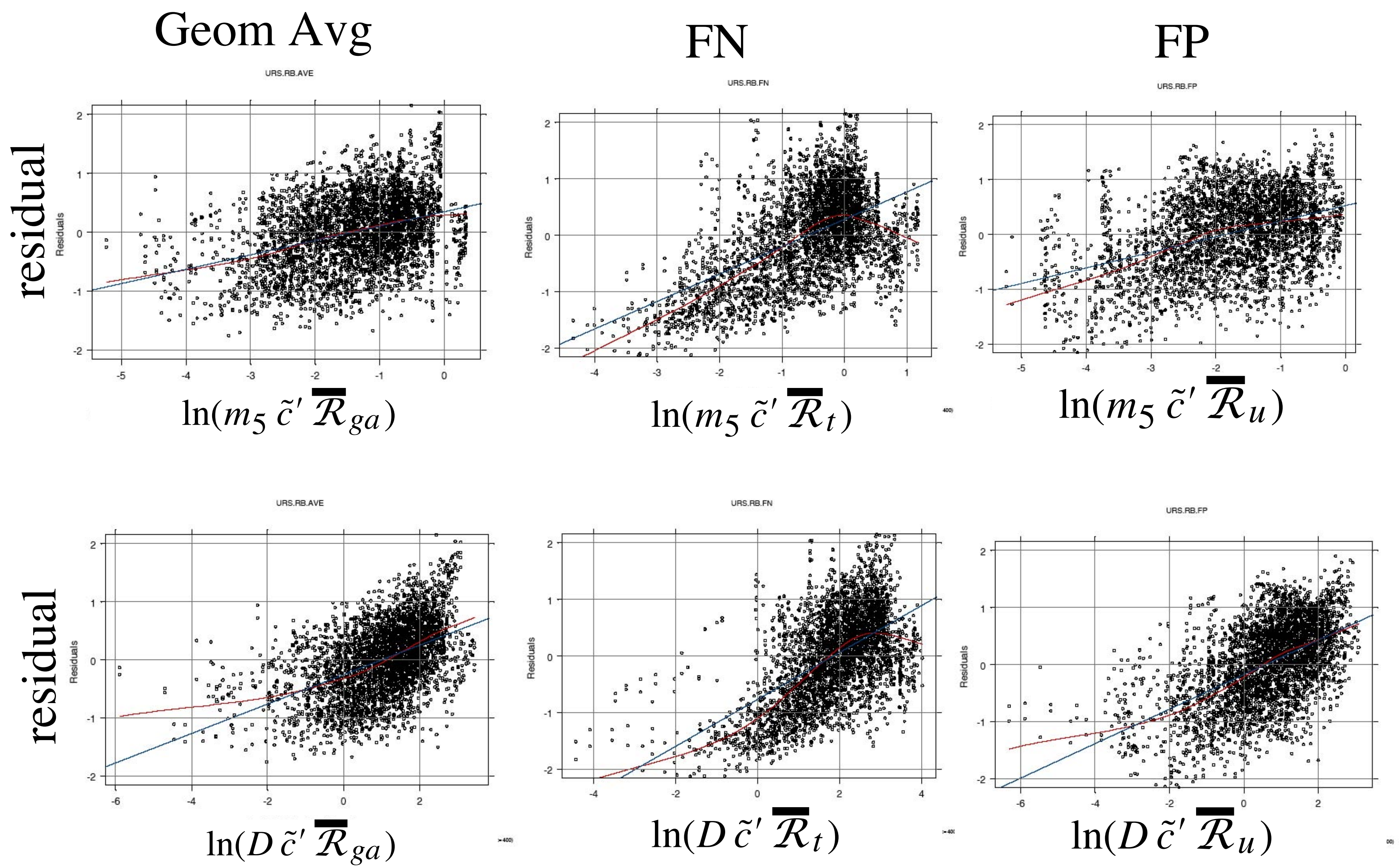

Figure 14

residual

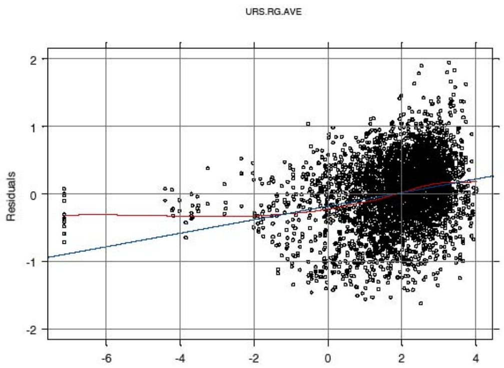

$\ln\left(D\,\tilde{c}'\,\overline{\mathcal{R}}_{ga}\right)$

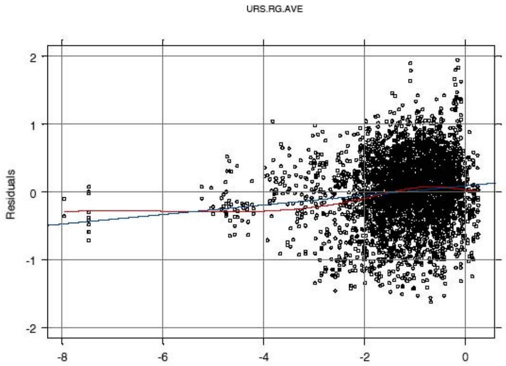

$\ln\left(m_5\,\tilde{c}'\,\overline{\mathcal{R}}_{ga}\right)$

RG, geom avg
comp

map of $\ln\left(D\,\tilde{c}'\,\overline{\mathcal{R}}_{ga}\right)$

map of $\ln\left(m_5\,\tilde{c}'\,\overline{\mathcal{R}}_{ga}\right)$

map of residuals

hypo
02

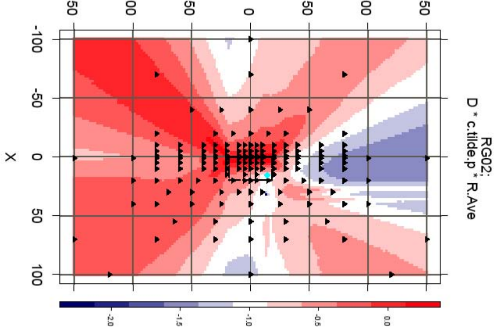

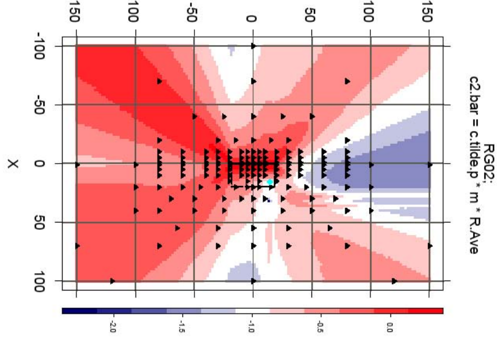

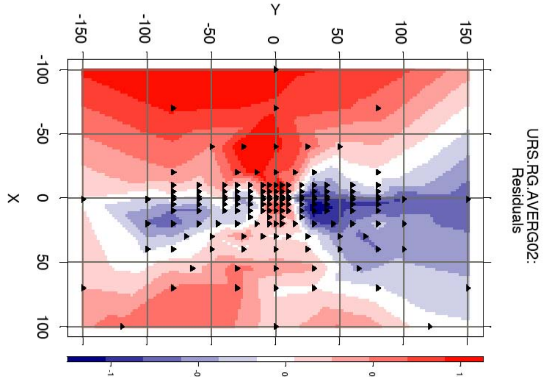

hypo
04

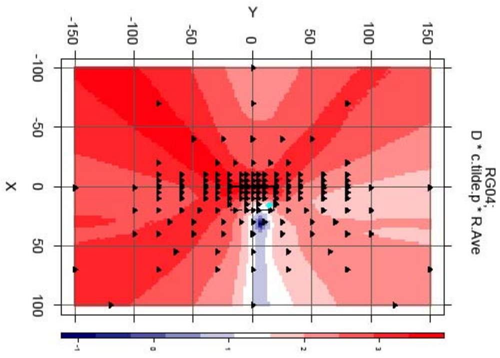

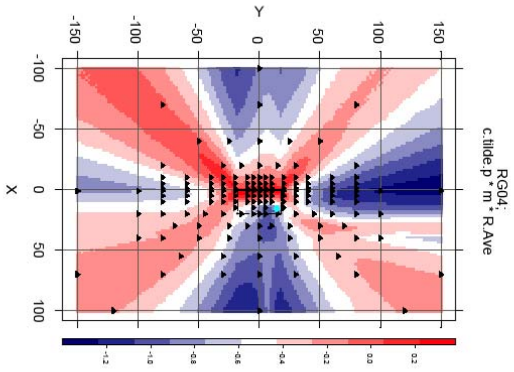

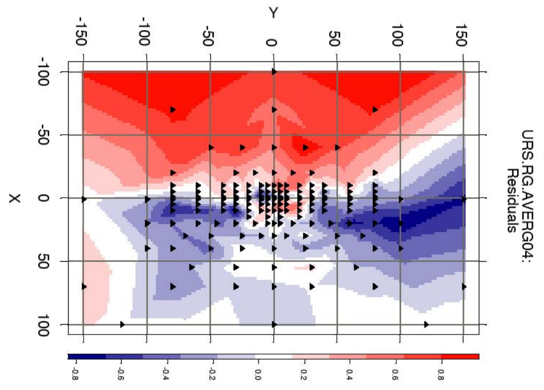

Figure 15

RG residuals vs two predictors

Geom Avg

FN

FP

residual

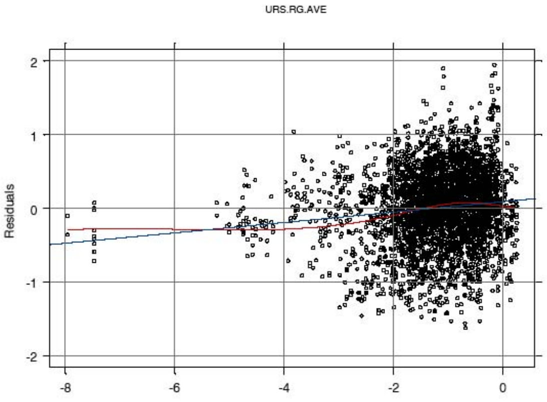

$\ln(m_5\, \tilde{c}'\, \overline{\mathcal{R}}_{ga})$

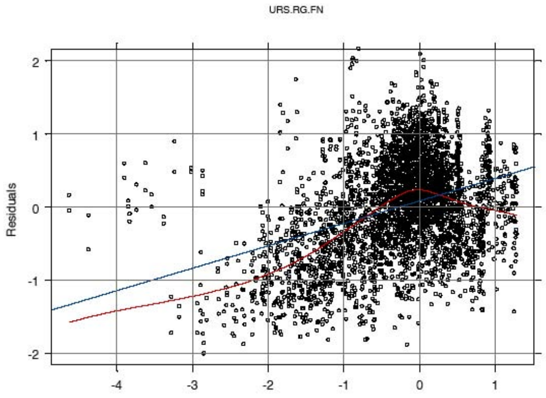

$\ln(m_5\, \tilde{c}'\, \overline{\mathcal{R}}_{t})$

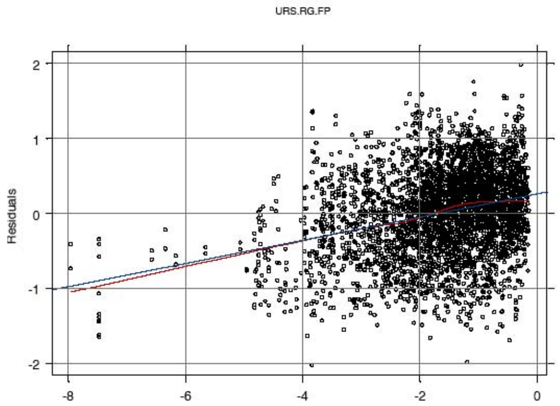

$\ln(m_5\, \tilde{c}'\, \overline{\mathcal{R}}_{u})$

residual

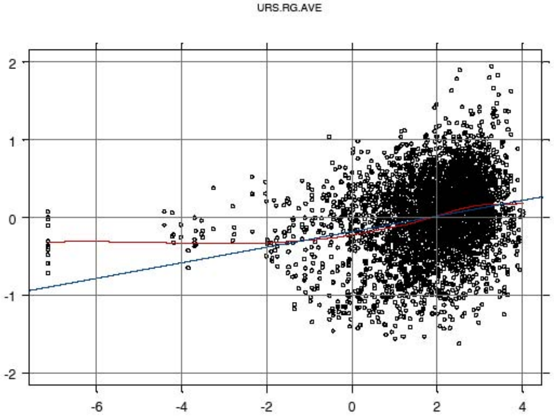

$\ln(D\, \tilde{c}'\, \overline{\mathcal{R}}_{ga})$

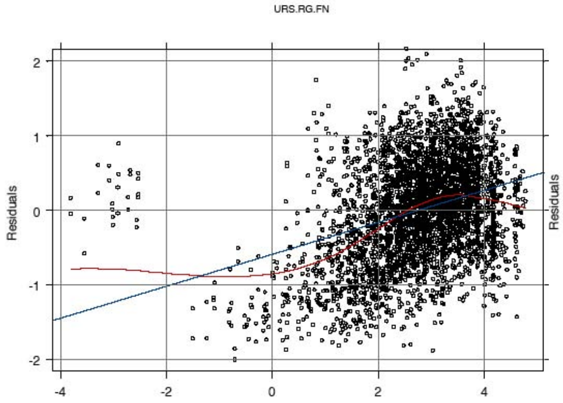

$\ln(D\, \tilde{c}'\, \overline{\mathcal{R}}_{t})$

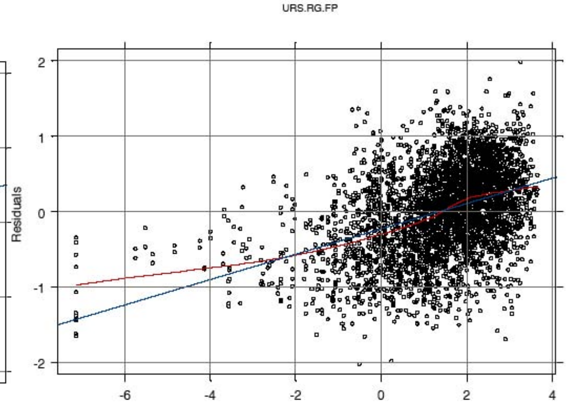

$\ln(D\, \tilde{c}'\, \overline{\mathcal{R}}_{u})$

Figure 16

residual

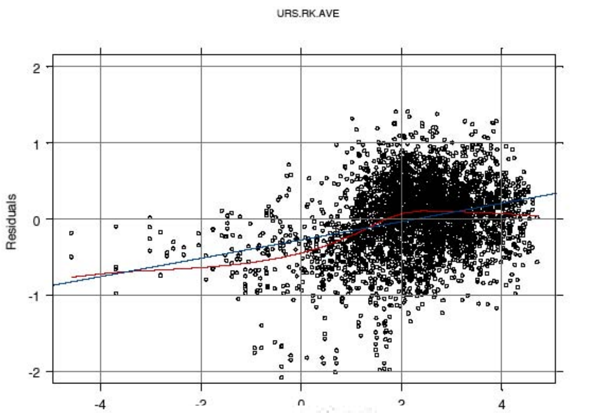

$\ln(D\,\tilde{c}'\,\overline{\mathcal{R}}_{ga})$

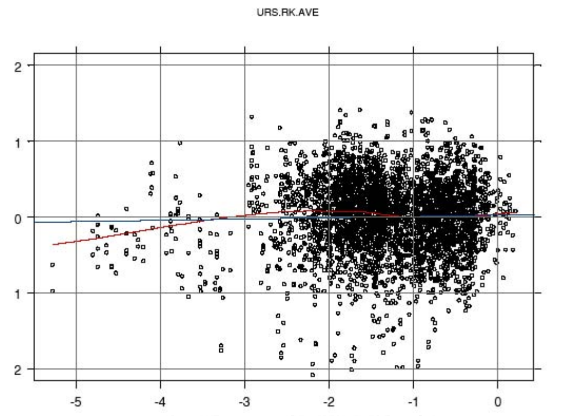

$\ln(m_5\,\tilde{c}'\,\overline{\mathcal{R}}_{ga})$

RK, geom avg comp

map of $\ln(D\,\tilde{c}'\,\overline{\mathcal{R}}_{ga})$

map of $\ln(m_5\,\tilde{c}'\,\overline{\mathcal{R}}_{ga})$

map of residuals

hypo 02

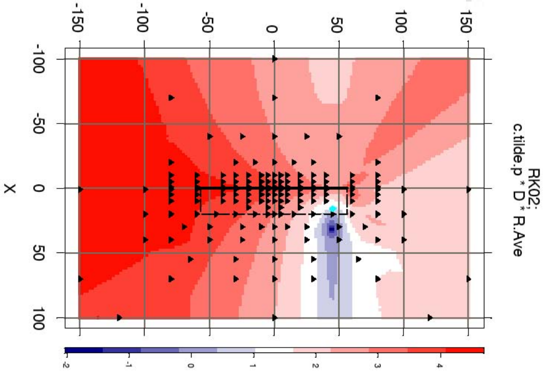

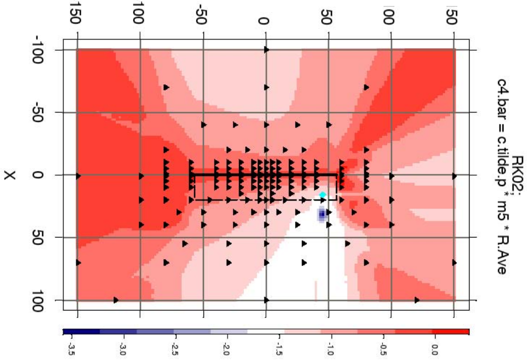

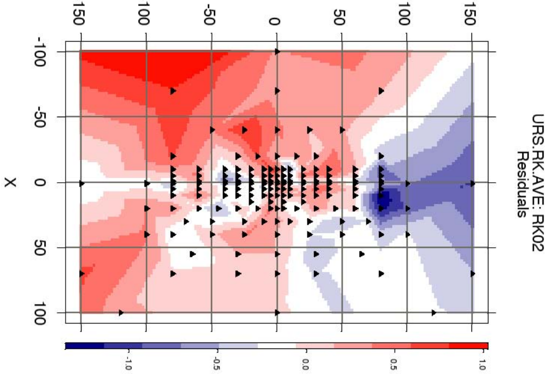

hypo 04

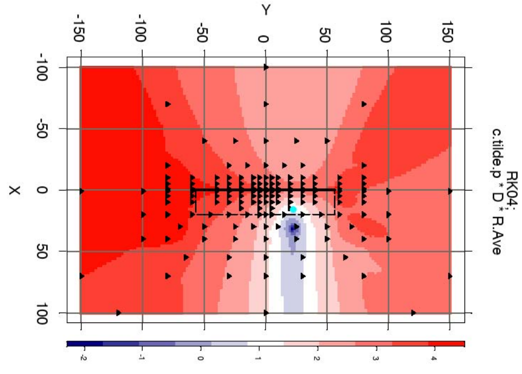

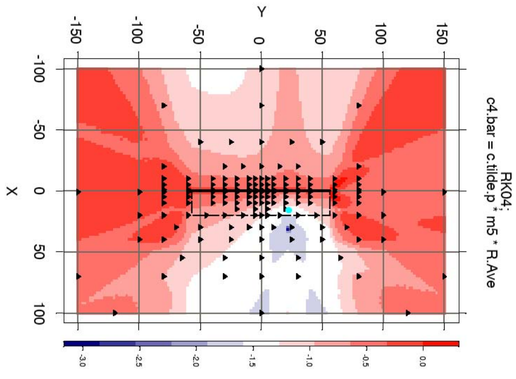

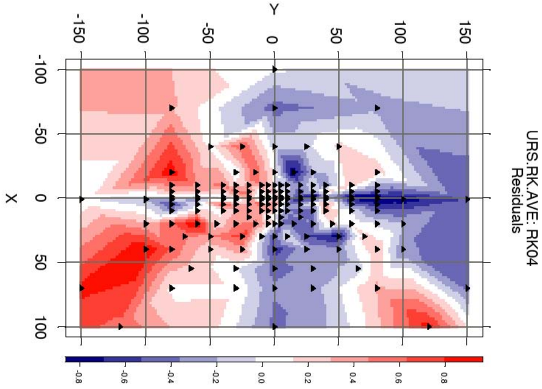

Figure 17

RK residuals vs two predictors

Geom Avg

FN

FP

residual

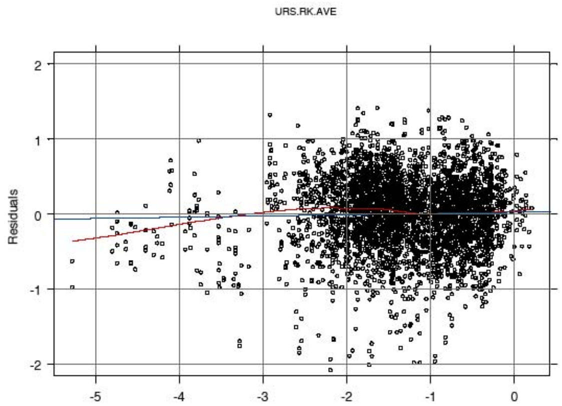

$\ln(m_5\,\tilde{c}'\,\overline{\mathcal{R}}_{ga})$

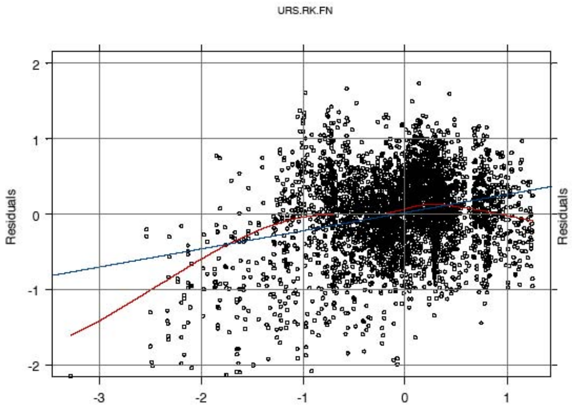

$\ln(m_5\,\tilde{c}'\,\overline{\mathcal{R}}_{t})$

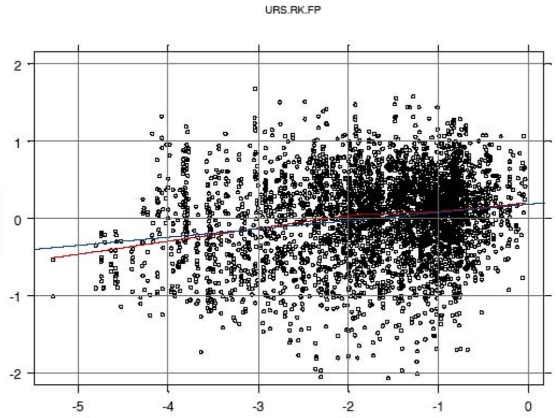

$\ln(m_5\,\tilde{c}'\,\overline{\mathcal{R}}_{u})$

residual

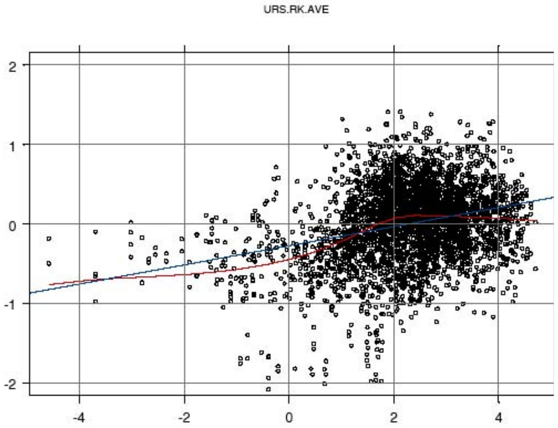

$\ln(D\,\tilde{c}'\,\overline{\mathcal{R}}_{ga})$

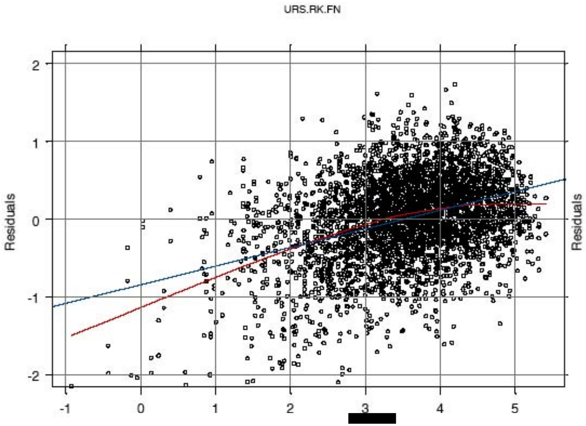

$\ln(D\,\tilde{c}'\,\overline{\mathcal{R}}_{t})$

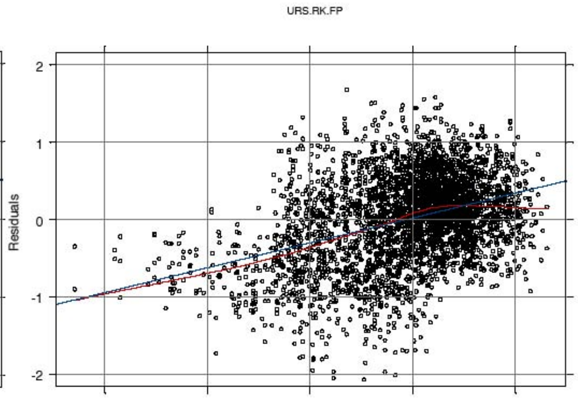

$\ln(D\,\tilde{c}'\,\overline{\mathcal{R}}_{u})$

Figure 18